JEM Journal of Experimental Medicine

ARTICLE

Lipid-loaded tumor-associated macrophages sustain tumor growth and invasiveness in prostate cancer

Michela Masetti[3*], Roberta Carriero[2*], Federica Portale[3], Giulia Marelli[3], Nicolò Morina[1,3], Marta Pandini[1,3], Marta Iovino[3], Bianca Partini[4], Marco Erreni[5], Andrea Ponzetta[6,7], Elena Magrini[6], Piergiuseppe Colombo[1,8], Grazia Elefante[8], Federico Simone Colombo[9], Joke M.M. den Haan[10], Clelia Peano[11,12,13], Javier Cibella[12], Alberto Termanini[2], Paolo Kunderfranco[2], Jolanda Brummelman[14], Matthew Wai Heng Chung[15], Massimo Lazzeri[16], Rodolfo Hurle[16], Paolo Casale[16], Enrico Lugli[14], Ronald A. DePinho[17], Subhankar Mukhopadhyay[15], Siamon Gordon[18,19], and Diletta Di Mitri[1,3]

Tumor-associated macrophages (TAMs) are correlated with the progression of prostatic adenocarcinoma (PCa). The mechanistic basis of this correlation and therapeutic strategies to target TAMs in PCa remain poorly defined. Here, single-cell RNA sequencing was used to profile the transcriptional landscape of TAMs in human PCa, leading to identification of a subset of macrophages characterized by dysregulation in transcriptional pathways associated with lipid metabolism. This subset of TAMs correlates positively with PCa progression and shorter disease-free survival and is characterized by an accumulation of lipids that is dependent on Marco. Mechanistically, cancer cell–derived IL-1β enhances Marco expression on macrophages, and reciprocally, cancer cell migration is promoted by CCL6 released by lipid-loaded TAMs. Moreover, administration of a high-fat diet to tumor-bearing mice raises the abundance of lipid-loaded TAMs. Finally, targeting lipid accumulation by Marco blockade hinders tumor growth and invasiveness and improves the efficacy of chemotherapy in models of PCa, pointing to combinatorial strategies that may influence patient outcomes.

Introduction

Cancer-related inflammation plays a crucial role in the progression of most cancer types. Components of both the innate and the adaptive immune system that are recruited upon tumor onset interact with each other and with the tumor, thus building an immune response in situ. Substantial evidence has shown that cancer cells can orchestrate this protumorigenic response by reprogramming the immune system (Biswas, 2015; Netea-Maier et al., 2018; Bezzi et al., 2018). Correspondingly, immune checkpoint inhibitors and restoration of adaptive antitumor immunity have shown strong efficacy in an ever-growing number of tumor types (Kyi and Postow, 2016; Lu et al., 2017; Sharma and Allison, 2015; Wei et al., 2017). The advent of molecular technologies, such as single-cell RNA sequencing (scRNA-seq) and associated computational analysis, has enabled unprecedented auditing of the composition of the tumor immune microenvironment. The immune landscape has been detailed for a number of cancers, including hepatocellular carcinoma, melanoma, non–small-cell lung cancer, kidney cancer, and breast cancer (Jaitin et al., 2019; Katzenelenbogen et al., 2020; Lavin et al., 2017; van Dijk et al., 2018; Zhang et al., 2019), revealing insights into the complexity and heterogeneity of the immune infiltrate, including novel immune players and previously unappreciated cell–cell interactions. We and others have similarly cataloged the immune microenvironment in human prostate

[1]Department of Biomedical Sciences, Humanitas University, Pieve Emanuele, Milan, Italy; [2]Bioinformatics Unit, Istituto di Ricovero e Cura a Carattere Scientifico Humanitas Research Hospital, Rozzano, Milan, Italy; [3]Tumor Microenvironment Unit, Istituto di Ricovero e Cura a Carattere Scientifico Humanitas Research Hospital, Rozzano, Milan, Italy; [4]Vita-Salute San Raffaele University, Milan, Italy; [5]Unit of Advanced Optical Microscopy, Istituto di Ricovero e Cura a Carattere Scientifico Humanitas Research Hospital, Rozzano, Milan, Italy; [6]Experimental Immunopathology Unit, Istituto di Ricovero e Cura a Carattere Scientifico Humanitas Research Hospital, Rozzano, Milan, Italy; [7]Center for Infectious Medicine, Department of Medicine Huddinge, Karolinska Institutet, Stockholm, Sweden; [8]Department of Pathology, Istituto di Ricovero e Cura a Carattere Scientifico Humanitas Research Hospital, Rozzano, Milan, Italy; [9]Flow Cytometry Core, Istituto di Ricovero e Cura a Carattere Scientifico Humanitas Research Hospital, Rozzano, Milan, Italy; [10]Department of Molecular and Cell Biology and Immunology, Amsterdam University Medical Center, Vrije Universiteit Amsterdam, Amsterdam, the Netherlands; [11]Human Technopole, Milan, Italy; [12]Genomics Unit, Istituto di Ricovero e Cura a Carattere Scientifico Humanitas Research Hospital, Rozzano, Milan, Italy; [13]Division of Genetic and Biomedical Research, UOS Milan, National Research Council, Rozzano, Milan, Italy; [14]Laboratory of Translational Immunology, Istituto di Ricovero e Cura a Carattere Scientifico Humanitas Research Hospital, Rozzano, Milan, Italy; [15]Medical Research Council Centre for Transplantation, Peter Gorer Department of Immunobiology, School of Immunology and Microbial Sciences, King's College London, London, UK; [16]Urology Unit, Istituto di Ricovero e Cura a Carattere Scientifico Humanitas Research Hospital, Rozzano, Milan, Italy; [17]Department of Cancer Biology, The University of Texas MD Anderson Cancer Center, Houston, TX; [18]Graduate Institute of Biomedical Sciences, College of Medicine, Chang Gung University, Taoyuan City, Taiwan; [19]Sir William Dunn School of Pathology, Oxford, UK.

*M. Masetti and R. Carriero contributed equally to this paper; Correspondence to Diletta Di Mitri: diletta.di_mitri@humanitasresearch.it.

adenocarcinoma (PCa), although these studies did not conduct a deep molecular analysis of the tumor immune infiltrate (Bezzi et al., 2018; Calcinotto et al., 2018; Di Mitri et al., 2019).

Tumor-associated macrophages (TAMs) are prominent components of the immune infiltrate in PCa and are known to foster cancer cell proliferation and invasiveness, enhance angiogenesis, and promote immunotolerance. TAMs also promote resistance to standard-of-care therapies as well as immunotherapies in certain contexts (Cassetta and Kitamura, 2018; Donadon et al., 2020; Gordon et al., 2017; Kaneda et al., 2016; Mantovani et al., 2017; Molgora et al., 2020; Noy and Pollard, 2014; Qian and Pollard, 2010). TAMs have been reported to induce resistance to chemotherapy in tumors, and depletion of TAMs improves the efficacy of docetaxel in castration-resistant prostate cancer (Guan et al., 2019; Salvagno et al., 2019). The development of clinical agents aimed at depleting TAMs or repolarizing them toward an antitumorigenic state remains a high priority but has been hampered by the complexity of the interplay between cancer cells and infiltrating macrophages.

The dysregulation of lipid metabolism in cancer cells plays a prominent role in tumor growth (Baenke et al., 2013; Munir et al., 2019). Similarly, the metabolic profile of macrophages can alter their functional state in a cancer-relevant manner (Batista-Gonzalez et al., 2020; Johnson et al., 2016; Niu et al., 2017; Rabold et al., 2017; Viganò et al., 2015; Vitale et al., 2019). For example, lipid accumulation in TAMs can drive an immunosuppressive phenotype that supports tumor progression (Wu et al., 2019). In PCa, de novo lipogenesis has been implicated in cancer development, and accordingly, inhibitors of fatty acid synthase restrict tumor growth (Kridel et al., 2004). Conversely, high-fat diet (HFD) in mouse models of PCa drives metastasis formation and appears to modulate immune infiltrates (Balaban et al., 2019; Chen et al., 2018; Hayashi et al., 2018; Narita et al., 2019; Stoykova and Schlaepfer, 2019; Watt et al., 2019). Such observations raise the possibility that lipid-related perturbations impact the immune microenvironment, including the molecular and functional state of macrophages in PCa.

To better define the composition and functional interactions in the tumor microenvironment of PCa, we conducted scRNA-seq to profile the immune infiltrate in human advanced PCa. These profiles and functional studies identified a subset of highly enriched lipid-loaded macrophages that correlates positively with cancer progression and decreased disease-free survival (DFS) and drive chemoresistance in a mouse model of PCa. Mechanistically, reciprocal cytokine signaling in the tumor microenvironment influences TAMs lipid metabolism and cancer cell migration and provides novel therapeutic targets for advanced PCa.

Results

High-dimensional single-cell profiling of the immune infiltrate in human PCa

To investigate the transcriptional landscape of TAMs, a 3′-based scRNA-seq strategy (10X Genomics) was applied to tissue-resident CD45$^+$ immune cells of freshly resected tumors from three treatment-naive PCa patients with a Gleason score equal to 9 (highly aggressive). CD45$^+$ immune cells were isolated from the tumor tissue and from the adjacent nontumor tissue of each patient (Fig. 1 A). We profiled 10,951 intratumor and 6,362 extratumor quality control–positive cells and applied the Seurat algorithm to generate a list of the most variable and differentially expressed genes for each cluster. We performed these analyses with manual annotation based on a cross-check of lineage-specific and cluster-enriched genes with available datasets. The SingleR algorithm was then used to assign each cluster to a known immune population (data not shown). The integration yielded cell-specific transcriptomic signatures that identified 18 clusters, including a variety of immune subsets, with a preponderance of cells of lymphoid origin (Fig. 1, B and C). Cluster (Cl) 12 was annotated as a nonimmune cluster, while Cl15, Cl16, and Cl17 were not annotated as they were composed by few events. As expected, there was a significant reorganization of the immune infiltrate in tumors compared with matched adjacent tissues. The most prominent changes detected in the tumor comprised a significant decrease of cancer-associated natural killer (NK) cells and a tendency to increase in tumor-infiltrating T regulatory (Treg) lymphocytes and dendritic cells (DCs), in line with previous reports (Fig. 1, D–G; Zhang et al., 2019). We identified two monocyte/macrophage subpopulations, Cl2 (Mac1) and Cl11 (Mac2), with Mac2 significantly enriched in the tumor tissue relative to normal tissue in all samples analyzed (Fig. 1 G). Among others, *NCAM1*, *CD68*, *CD163*, and *CD14* were used as monocyte/macrophage-defining genes.

TAMs show dysregulation of lipid metabolism–associated pathways

To further dissect the molecular features of TAMs in our samples, we explored the biological pathways that were associated with the Mac1 and Mac2 clusters in both normal and tumor conditions. Ingenuity Pathway Analysis (IPA) revealed that processes related to lipid metabolism and lipid intake, including PPAR signaling, VDR/RXR activation, atherosclerosis signaling, and LXR/RXR activation pathways, showed an enrichment in Mac2 compared with Mac1 (Fig. 2 A). Some of these processes were further enriched in the intratumor Mac2 (itMac2) compared with its normal counterpart (nMac2), thus indicating that the tumor microenvironment has an impact on the transcriptome of infiltrating macrophages (Fig. 2 A). Comparison of the transcriptional profile of the itMac2 with nMac2 (Fig. S1 A) identified 718 differentially expressed genes ($P < 0.05$). Metallothioneins (*MT1B*, *MT1M*), osteopontin-1 (*SPP1*), chitinase-3–like protein 1 (*CHI3L1*), metalloproteins (*TIMP-1*), and scavenger receptors (*MARCO*, *OLR1*) were among the most upregulated genes in the itMac2 (Fig. S1 A). In addition, gene set enrichment analysis (GSEA) applied to the itMac2 cluster showed the enrichment of a gene signature recently linked to a subset of macrophages associated with adipose tissue (normalized enrichment score = 1.92, false discovery rate q value = 0.008; Fig. S1 B; Jaitin et al., 2019). This profile is consistent with the changes in lipid-associated pathways detected in the Mac2 cluster. We then performed an additional comparison inquiry between the Mac1 and Mac2 macrophage clusters (Fig. 2, B and C). IPA performed on genes that were differentially expressed in

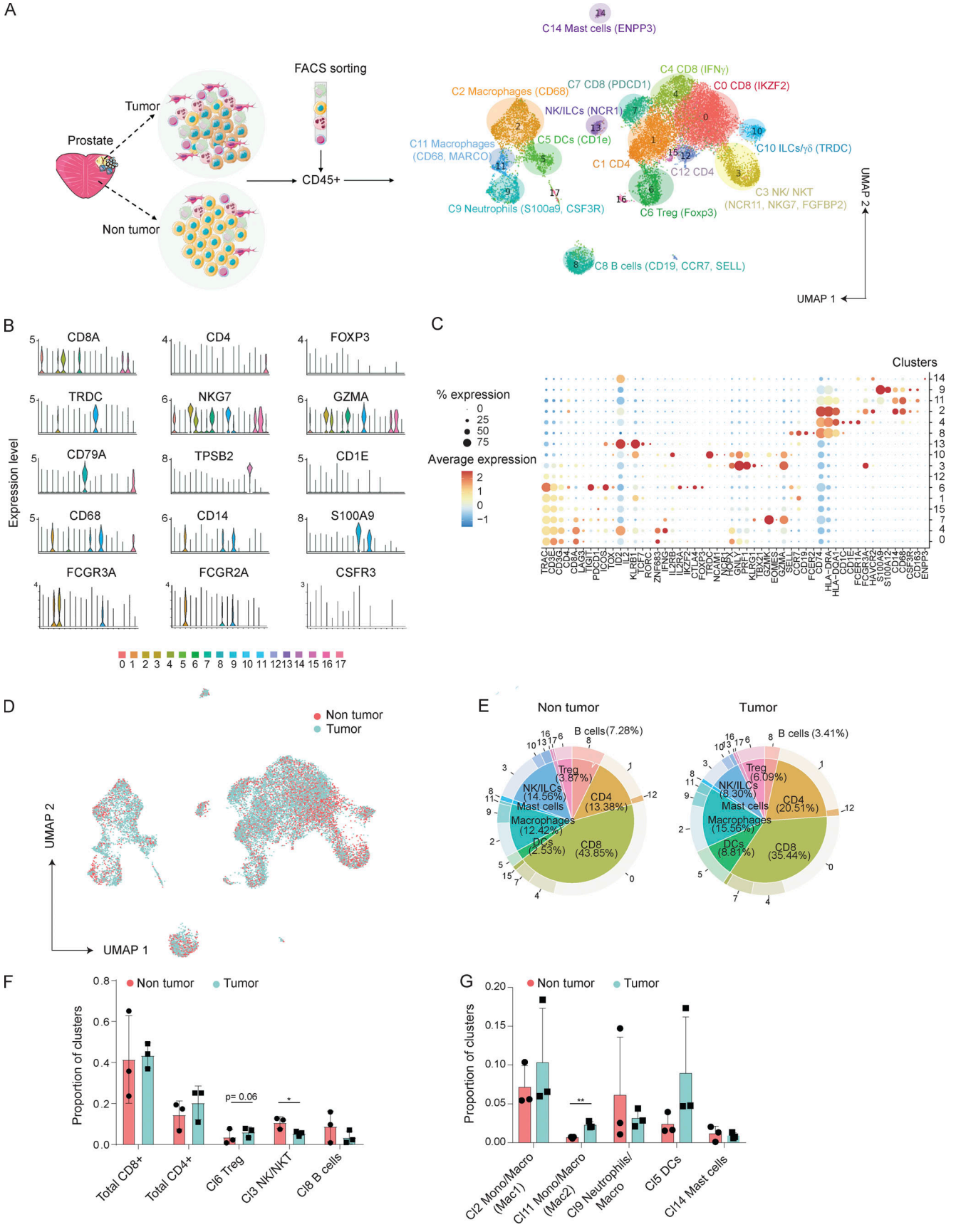

Figure 1. **High-dimensional single-cell profiling of the immune infiltrate in PCa patients. (A)** Workflow of the experimental approach. 3′-based scRNA-seq was applied to the CD45+ infiltrating cells from tumor and nontumor adjacent PCa tissue (three patients). CD45+ immune cells were isolated by FACS

sorting. Identification of immune clusters in prostate (tumor and normal). Uniform manifold approximation and projection (UMAP) of CD45⁺ cells in prostate (tumor and normal adjacent tissue). 18 clusters characterized by lineage-specific and cluster-enriched genes were identified by integrated analysis. **(B)** Violin plot showing expression of lineage-specific genes in each cluster. **(C)** Dot plot showing expression levels of lineage-specific marker genes. **(D)** UMAP showing tissue distribution (tumor and nontumor tissue) of CD45⁺ cells. **(E)** Pie charts of the relative percentages of immune cell clusters in tumor and normal tissue. **(F and G)** Proportion of different immune cell clusters between tumor and normal prostatic tissue. We identified cluster 9, representative of NK cells, as being significantly downregulated in tumor tissue (F), whereas macrophagic cluster 11 was significantly increased in tumor tissue (G). Data in F and G are expressed as mean ± SD. Student *t* test was performed (F). *, P < 0.05; **, P value < 0.01. ILC, innate lymphoid cell; Macro, macrophage; Mono, monocytes.

the Mac2 compared with the Mac1 cluster (n = 479: 365 upregulated and 114 downregulated; adjusted P < 0.05) reported 176 enriched pathways (P < 0.05). In accordance with the data shown above, processes associated with lipid metabolism and modulation of lipid intake showed an enrichment in Mac2 (Fig. 2 D).

To explore more deeply the possible heterogeneity among the broadly defined macrophage subsets, we performed reclustering of macrophage clusters, considering Cl2, Cl9, and Cl11. After clearing unwanted cells, we could better discriminate myeloid subpopulations. Seurat algorithm analysis discriminated five clusters of macrophages, one cluster of monocytes, and one cluster of neutrophils, which we defined as follows on the basis of differentially expressed genes: Cl0-CCL3_Mac, Cl1-C1Q_Mono, Cl2-S100a9_Mac, Cl3-MARCO_Mac, Cl4-THBS1_Neutrophils, Cl5-IFITM2_Mac, and Cl6-STMN1_Mac (Fig. S1 C). One subset composed of contaminating T cells was excluded from the analysis. Among the clusters, Cl3-MARCO_Mac was the only subset significantly enriched in the tumor versus normal tissue (Fig. S1 D). To deeply dissect MARCO_Mac specifically in the tumor context, we applied the same approach, considering only the tumor counterpart (Fig. 2 E). Starting from tumor reclustering, we then used a Monocle3 algorithm to determine gene expression changes occurring among tumor macrophage subpopulations. The trajectory was inferred based on gene expression changes of cells belonging to different clusters, and pseudotime was estimated as a measure of progression of cells through biological processes. This analysis identified MARCO_Mac as a cluster with a different path through the trajectory and a high pseudotime value, suggesting that this subset possesses a distinct functional profile (Fig. 2, E and F). Cl11-Mac2 subset from the merge analysis is mostly composed of cells belonging to MARCO_Mac of reclustering, while Cl22-Mac1 is composed of CCL3_Mac, C1Q_Mono, and STMN1_Mac (Fig. S1 E). As mentioned, MARCO_Mac showed a higher pseudotime value, thus indicating that Mac2 may be more mature than Mac1. To further investigate the myeloid clusters, we analyzed modules of coregulated genes assigned to each cluster along the trajectory. This step provided a means to collect sets of genes that vary across the clusters. Functional analysis of module genes showed a specific enrichment of module 6 in MARCO_Mac (Fig. 2 G), driving biological pathways related to perturbations of lipid metabolism and lipid intake, including LXR/RXR activation, FXR/LXR activation, and atherosclerosis signaling, in accordance with the data shown above (Fig. 2 H). In summary, we applied two different strategies to analyze scRNA-seq of human PCa, both converging on identification of a subset of tumor-infiltrating macrophages, defined as MARCO_Mac, that is characterized by a transcriptional perturbation in lipid-related pathways.

MARCO_Mac defines a macrophage subset with a prognostic significance in human PCa

Recent evidence highlighted the importance of MARCO as a prototypic marker of TAMs, even if the mechanistic insight into this expression is lacking (Lavin et al., 2017). Our computational identification of MARCO-expressing TAMs with activation of lipid-related pathways prompted experimental validation of the lipid content of TAMs in PCa. To this end, multicolor immunofluorescence staining was performed on tumor sections from PCa patients, comparing intratumor and adjacent nontumor tissues. Strong accumulation of lipids was detected in the cytoplasm of CD68⁺ cells exclusively in intratumor regions as documented by expression of adipophilin (ADFP), a protein expressed on the membrane of cytoplasmic lipid droplets (Persson et al., 2007; Robenek et al., 2006; Straub et al., 2013), and BODIPY (Fig. 2, I and J; and Fig. S1, F–H). As described above, MARCO was identified as a distinctive marker of TAMs (Fig. 3 A). Since MARCO has been implicated in the uptake of modified lipoproteins (Elshourbagy et al., 2000), we hypothesized that this scavenger receptor may be involved in the augmented lipid content in TAMs in PCa. To test this, we performed immunofluorescence staining to visualize MARCO in the tumor tissue of PCa patients. Accordingly, immunofluorescence staining documented MARCO signal in CD68⁺ TAMs (Fig. 3 B; and Fig. S1, I and J), and BODIPY staining of the lipid content of cells (Fig. 3 C) correlated with MARCO expression, implying a link between MARCO and lipid accumulation in TAMs in PCa. Importantly, *MARCO* gene expression was shown to correlate with the expression of genes implicated in the regulation of lipid metabolism when analyzed in PCa patients from The Cancer Genome Atlas (TCGA) dataset (Fig. S1 K). Correspondingly, the human TCGA PCa dataset showed a significant positive correlation between expression of *MARCO* and the panmacrophage marker *CD68* (Fig. 3 D). Importantly, *MARCO* expression was associated with tumor progression in PCa, being significantly higher in patients affected by high-grade cancer (Gleason score = 9–10) compared with low-grade disease (Gleason score = 6; Fig. 3 E). Consistent with this, *MARCO* expression significantly correlated with *PTEN* loss in PCa patients, with *PTEN* being a driving mutation in human PCa, indicative of more-advanced disease (Fig. 3 F; Jamaspishvili et al., 2018). We then investigated the association between *MARCO* expression and *TRP53* and *RB1* loss that are common genetic alterations in advanced prostate cancer, but we could not detect any significant correlation (Fig. S1, L and M). Such findings reinforce the notion that the genetic background of tumors may impact the transcriptional profile of

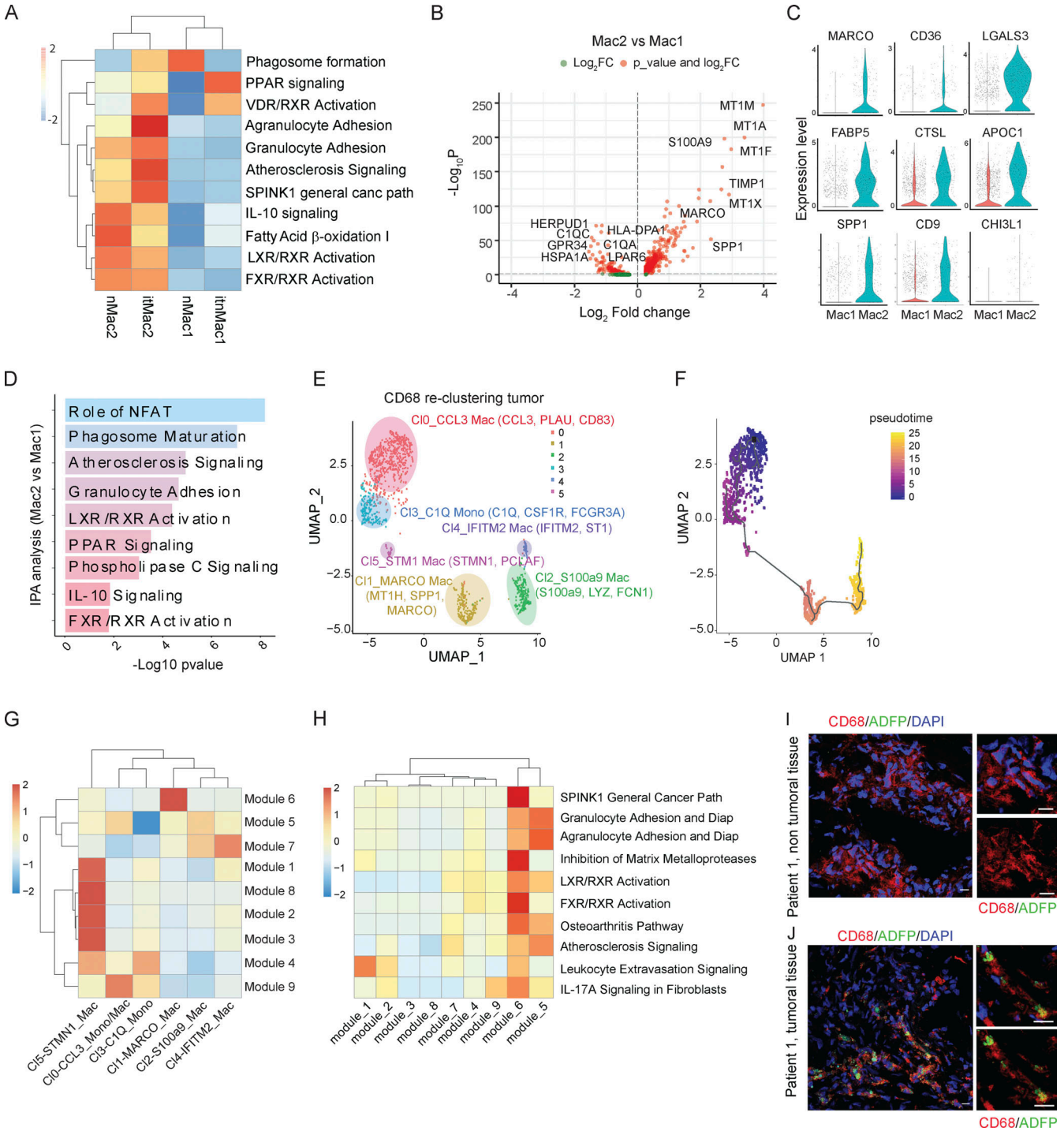

Figure 2. **Tumor-enriched macrophages show a dysregulation of lipid metabolism–associated pathways. (A–C)** Differential expression analysis between Mac1 and Mac2. **(A)** Heat map showing enriched IPA pathways in itMac2 and itMac1 and nMac2 and nMac1 deriving from differential expression analysis of Mac2 and Mac1 versus all the other clusters in both normal and tumor conditions. Enrichment scores are provided as $-\log_{10}$ P value and scaled by row. **(B)** Volcano plot showing differential expressed genes between Mac1 and Mac2. Genes are colored according to their $\log_2$FC value. **(C)** Violin plots showing normalized expression levels of selected up-regulated genes in Mac2 with respect to Mac1. **(D)** IPA of differentially expressed genes between Mac2 and Mac1 clusters. Selected significant pathways are shown according to $-\log_{10}$ P value threshold >1.3. **(E)** Uniform manifold approximation and projection (UMAP) representing reclustering of tumor cells belonging to Cl2, Cl9, and Cl11. **(F)** Monocle trajectory analysis of macrophage clusters in tumor. Cells are colored according to their pseudotime value. **(G)** Heat map showing the Monocle trajectory analysis of tumor macrophage clusters. Module enrichment value is reported along the different clusters and scaled by column. **(H)** Heat map representing the most functional relevant pathways according to IPA annotation enriched in module 6. Enrichment scores are provided as −log10 P values. A specific enrichment of module 6 with genes associated with lipid metabolism and lipid intake in MARCO_Mac was observed. **(I and J)** Representative confocal immunofluorescence images of human PCa from non-tumor–adjacent tissue (I) and tumor tissue (three patients were analyzed). Scale bar, 10 µm (10 µm for digital zoom). Red-stained CD68$^+$ macrophages colocalize with green-stained ADFP lipid droplets in the tumor tissue (J). Images were acquired with an SP8-II confocal microscope (Leica) with a 40× objective. Images on the right are 2× digital zoom. Nuclei were counterstained with DAPI (blue). canc path, cancer pathway; Diap, diapedesis.

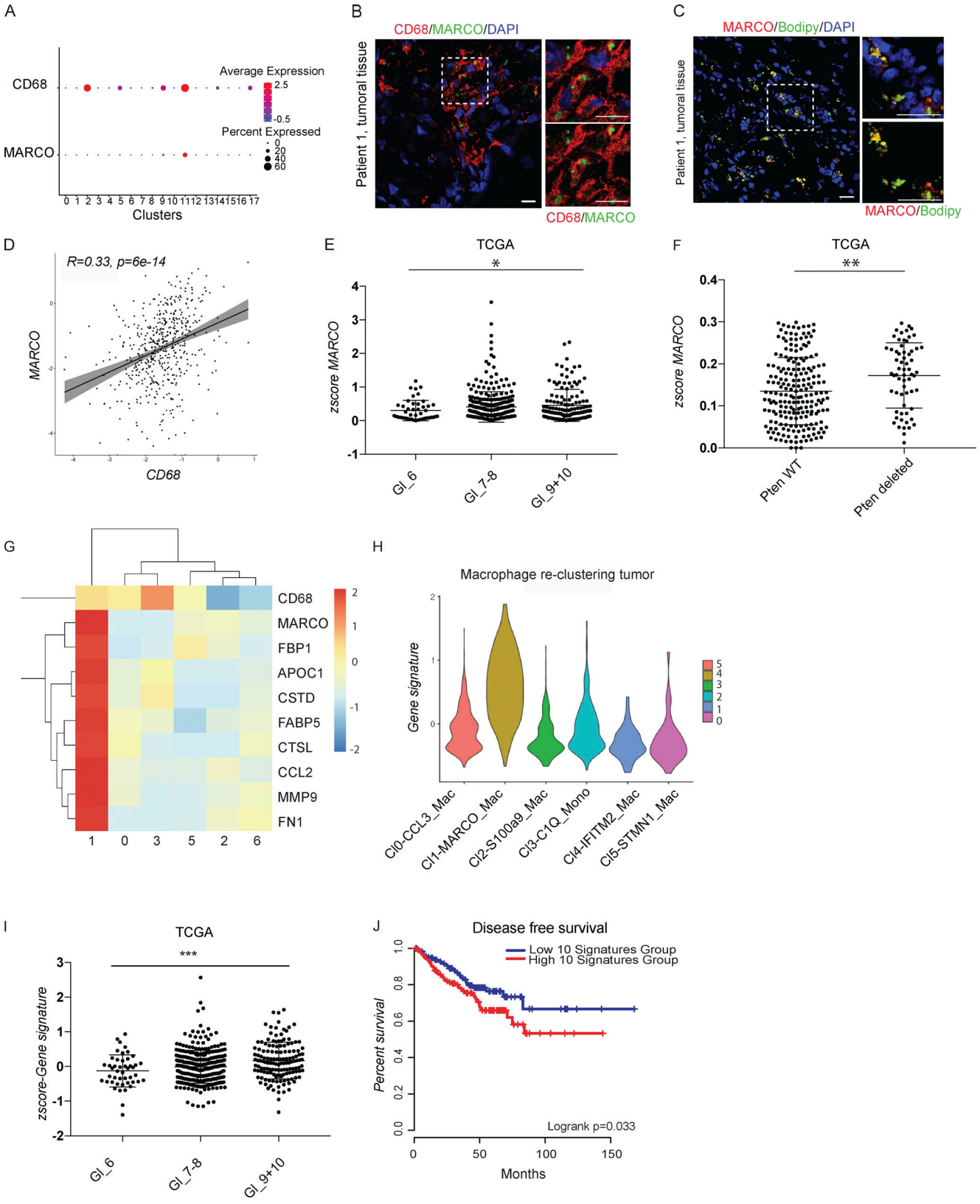

Figure 3. **MARCO_Mac defines a macrophage subset with a prognostic significance in human PCa. (A)** Dot plot showing the proportion of cells along the 18 clusters expressing *CD68* and *MARCO* (dot size), according to their average expression (color scale). **(B)** Representative confocal immunofluorescence images of human PCa tumor tissue. Red-stained CD68⁺ macrophages colocalize with green-stained MARCO cells. Images were acquired with an SP8-II confocal microscope (Leica) with a 40× objective. Images on the right are 2× digital zoom. Nuclei were counterstained with DAPI (three patients were analyzed). Scale bar, 10 µm (10 µm for digital zoom). **(C)** Representative confocal immunofluorescence images of human PCa tumor tissue. Red-stained MARCO⁺ macrophages

colocalize with green-stained BODIPY lipids (lipid droplets). Images were acquired with an SP8-II confocal microscope with a 40× objective. Images on the right are 2× digital zoom. Nuclei were counterstained with DAPI (three patients were analyzed). Scale bar, 20 µm (20 µm for digital zoom). **(D)** Pearson's correlation showing a positive correlation between *MARCO* and *CD68* in the TCGA human PCa dataset. Gene expression values are provided as FPKM. **(E)** Correlation of *MARCO* gene expression with Gleason score in PCa patients from the TCGA dataset. Unpaired *t* test (*, P ≤ 0.04). **(F)** Correlation of *MARCO* expression levels with *PTEN* loss in the TCGA cohort. Gene expression values are provided as FPKM. Unpaired *t* test (**, P ≤ 0.0013). **(G)** Heat map showing the cluster-specific gene signature based on differentially expressed genes that modulate the functional state of MARCO_Mac. **(H)** Violin plot representing gene signature score of MARCO_Mac cluster along tumor macrophage clusters. **(I)** Correlation of MARCO_Mac gene signature with Gleason score in PCa patients from TCGA dataset. Gene signature is provided as normalized *z* score. One-way ANOVA (***, P ≤ 0.008). **(J)** DFS analysis of TCGA cohort divided by the median expression value of MARCO_Mac gene signature. DFS analysis was performed by Gepia2 Web tool. Gl, Gleason. Data in E, F, and I are expressed as mean ± SD.

infiltrating TAMs in accordance with previous evidence (Bezzi et al., 2018). Finally, we confirmed the association of *MARCO* expression with tumor progression in an additional cohort of PCa patients (Fig. S1 N; Taylor et al., 2010). On this foundation of evidence, we derived a cluster-specific gene signature based on differentially expressed genes that modulate the functional state of MARCO_Mac (Fig. 3 G). This signature clearly discriminates the MARCO_Mac cluster in the reclustering of myeloid cells and in the total immune infiltrate (Fig. 3 H and Fig. S1 O). Interestingly, the expression of the MARCO_Mac gene signature was associated with Gleason score in both the TCGA and Taylor datasets (Fig. 3 I and Fig. S1 P). In addition, the MARCO_Mac gene signature significantly correlated with *PTEN* loss (Fig. S1 Q) and DFS in the TCGA cohort (Fig. 3 J). Together, these results indicate that MARCO is a TAM-associated marker potentially involved in PCa progression and that MARCO_Mac defines a macrophage subset with a prognostic significance in human PCa.

The abundance of lipid-loaded TAMs correlates positively with tumor aggressiveness in murine models of PCa

To further investigate the interplay between TAMs and prostate cancer cells, we used two well-characterized genetically engineered mouse models of PCa that recapitulate low versus high tumor aggressiveness in human PCa. The $Pten^{pc-/-}$ model develops organ-confined tumors resembling poorly progressive human prostatic intraepithelial neoplasia (Alimonti et al., 2010), whereas the $Pten^{pc-/-}$; $Smad4^{pc-/-}$ model develops aggressive adenocarcinoma that becomes invasive at 12 wk of age and metastatic to lymph nodes and lungs after 15 wk of age (Ding et al., 2011). In accordance with previous findings, both mouse models possessed a heterogeneous infiltration of immune subsets, with the $Pten^{pc-/-}$; $Smad4^{pc-/-}$ model characterized by a significant increase of $CD45^+F4/80^-LY6G^+$ neutrophils compared with the $Pten^{pc-/-}$ (Fig. 4, A and B). To profile macrophages in these models, $CD45^+F4/80^+LY6G^-$ macrophages were sorted from the prostatic tumors and subjected to RNA-seq to define their transcriptional landscape (Fig. 4 C). Differential analysis revealed an altered transcriptional profile of macrophages in the $Pten^{pc-/-}$; $Smad4^{pc-/-}$ metastatic model (met_Mac) compared with macrophages from the $Pten^{pc-/-}$ organ-confined model (oc_Mac; 109 upregulated and 157 downregulated genes; P < 0.05, log_2-fold change [log_2FC] > |1.5|). Notably, MARCO was upregulated in met_Mac versus oc_Mac (P = 0.03, log_2FC = 2.46; Fig. 4, D and E). In addition, IPA of differentially expressed genes highlighted the upregulation of pathways associated with lipid metabolism and intake, in accordance with human data (Fig. 4 F).

Next, we explored the lipid content of intratumor macrophages in the $Pten^{pc-/-}$ and $Pten^{pc-/-}$; $Smad4^{pc-/-}$ models, with Pten WT noncancerous prostates used as control. Flow cytometry analysis detected the infiltration of $ADFP^+$ lipid-loaded TAMs in the prostatic tumors, which were nearly absent in the normal prostate, a finding confirmed by immunofluorescence staining (Fig. 4, G–I; and Fig. S2, A and B, with Fig. 4 I showing a higher magnification of Fig. S2 A). Of note, the abundance of lipid droplets in TAMs was significantly enriched in the metastatic model versus the organ-confined model, consistent with the notion that the lipid content of tumor-infiltrating macrophages correlates positively with tumor progression. In addition, immunofluorescence staining showed the association between ADFP positivity and MARCO expression in $Pten^{pc-/-}$; $Smad4^{pc-/-}$ tumors, consistent with our human data (Fig. S2 C). Of note, ADFP expression was almost absent in tumor-infiltrating neutrophils, thus indicating that lipid loading is a signature feature of TAMs in these settings (Fig. S2 D). Consistent with previous findings that lipid accumulation polarizes macrophages toward a $CD206^+$ protumorigenic phenotype (Wu et al., 2019), FACS analysis confirmed that $CD206^+$ TAMs express higher levels of ADFP in our PCa model (Fig. S2 E). Importantly, *MARCO* expression correlates with the expression of *CD206* in the TCGA cohort (Fig. S2 F) and in our human dataset (Fig. S2, G and H).

Finally, to further confirm our findings in orthotopic models of PCa, we used PCa cell lines derived from the prostatic epithelia of the $Pten^{pc-/-}$ and $Pten^{pc-/-}$; $Smad4^{pc-/-}$ conditional mouse models (Ding et al., 2011; see Materials and methods) as follows: the $Pten^{-/-}$ cells (nonmet cells) derive from the organ-confined prostatic adenocarcinoma ($Pten^{pc-/-}$), whereas the $Pten^{-/-}$; $Smad4^{-/-}$ cells (met cells) derive from the advanced metastatic adenocarcinomas ($Pten^{pc-/-}$; $Smad4^{pc-/-}$). Murine PCa cell lines were injected in one anterior lobe of a recipient mouse, while the symmetric lobe was injected with saline. The myeloid immune infiltrate of injected tumors mirrored that of the conditional mouse tumors from which the cell lines originated. Indeed, also in these models, we observed a reduction of infiltrating macrophages in the $Pten^{-/-}$; $Smad4^{-/-}$ orthotopic tumor and a significant increase in neutrophils compared with the $Pten^{-/-}$ tumors (Fig. S2, I and J). FACS analysis of tumor infiltrates at 45 d after injection revealed the appearance of lipid-loaded macrophages infiltrating the $Pten^{-/-}$; $Smad4^{-/-}$ tumor mass, which were absent in the WT lobe and scarce in the $Pten^{-/-}$-injected lobes (Fig. 4 J). Lipid-loaded $ADFP^+$ macrophages showed a higher expression of Cd206, Pdl1, Cd36, and Cd39 than $ADFP^-$ TAMs (Fig. S2 K). These data indicate that lipid

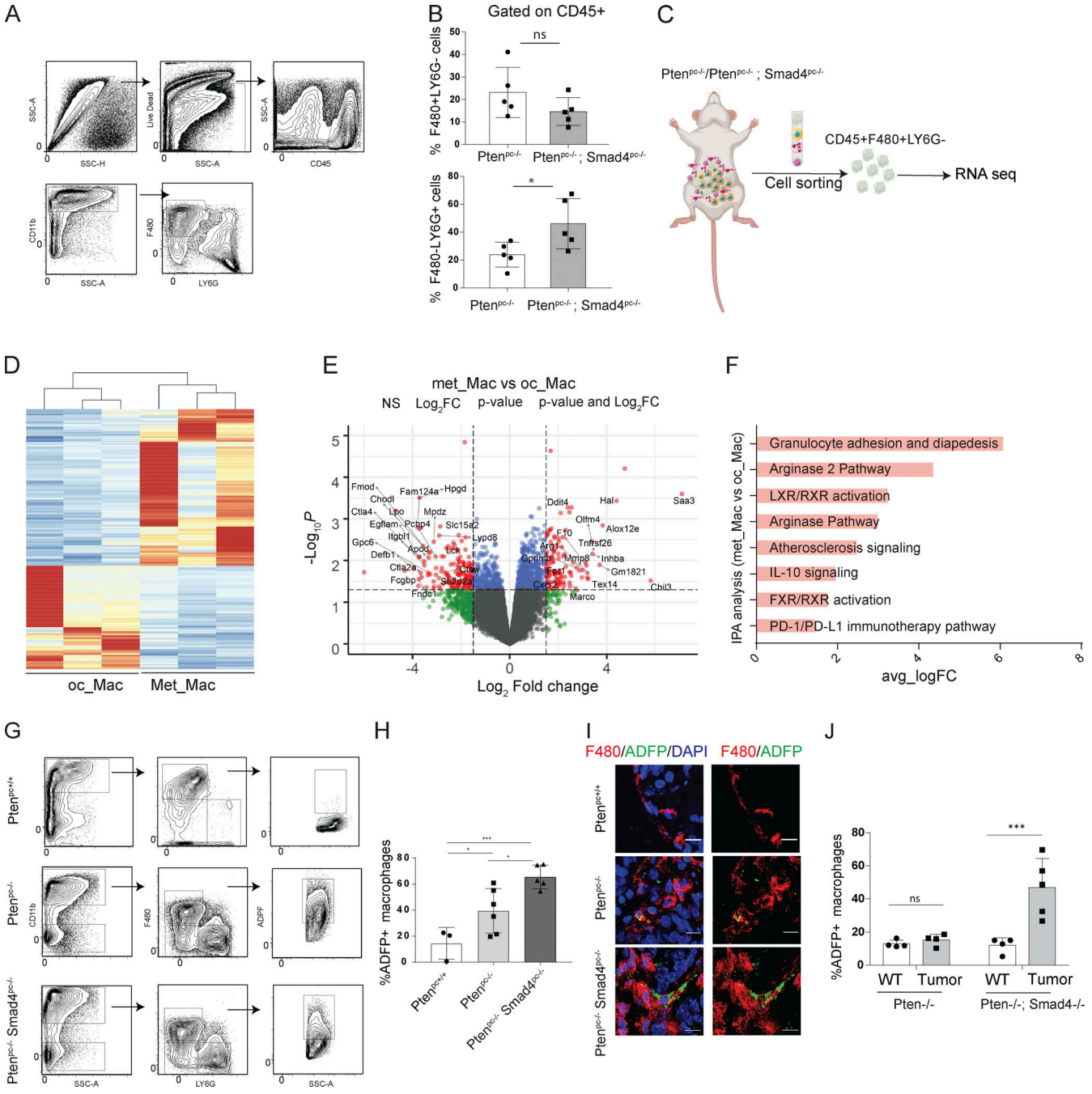

Figure 4. **The abundance of lipid-loaded TAMs is associated with tumor progression in murine models of PCa. (A)** Gating strategy for identification of TAMs and neutrophils. *n* = 5/group. **(B)** Bar graphs showing the frequency of macrophages and neutrophils, gated on CD45$^+$ cells. **(C)** Workflow of TAM sorting from transgenic mice and subsequent RNA-seq. **(D)** RNA-seq analysis performed on TAMs (CD45$^+$F4/80$^+$Ly6G$^-$) isolated from Pten$^{pc-/-}$ and Pten$^{pc-/-}$; Smad4$^{pc-/-}$ tumors. *n* = 3/group. Heat map showing normalized gene expression values of significant modulated genes. **(E)** Volcano plot showing differentially expressed genes between TAMs isolated from Pten$^{pc-/-}$ (oc_Mac) and Pten$^{pc-/-}$; Smad4$^{pc-/-}$ (met_Mac) tumors. Genes are colored according to their $\log_2$FC values. **(F)** IPA of differentially expressed genes between met_Mac and oc_Mac. Significant canonical pathways are represented according to their $-\log_{10}$ P value. **(G)** Gating strategy used to identify lipid-loaded TAMs in murine prostatic tumors. CD11b$^+$ cells were gated on previously gated viable and CD45$^+$ cells. ADFP expression was evaluated on macrophages identified as F4/80$^+$Ly6G$^-$ cells on CD11b$^+$CD45$^+$ previously gated cells. **(H)** Frequency of ADFP$^+$ TAMs in prostates from WT (Pten$^{pc+/+}$) mice or Pten$^{pc-/-}$ and Pten$^{pc-/-}$; Smad4$^{pc-/-}$ transgenic animals. Data are mean ± SE. *n* = 3 for WT (Pten$^{pc+/+}$) prostates, *n* = 6 for Pten$^{pc-/-}$, and *n* = 5 for Pten$^{pc-/-}$; Smad4$^{pc-/-}$ tumors. **(I)** Representative confocal immunofluorescence images of tumor anterior prostate lobes from WT (Pten$^{pc+/+}$), Pten$^{pc-/-}$, and Pten$^{pc-/-}$; Smad4$^{pc-/-}$ mice. Red-stained F4/80$^+$ macrophages colocalize with green-stained ADFP lipid droplets in the Pten$^{pc-/-}$; Smad4$^{pc-/-}$ tumors. Images were acquired with an SP8-II confocal microscope (Leica) with a 40× objective. Images are 2× digital zoom. Nuclei were counterstained with DAPI. Scale bar, 10 µm. **(J)** Frequency of ADFP$^+$ TAMs in the orthotopic models of prostate cancer. Murine prostate cancer cell lines (Pten$^{-/-}$ or Pten$^{-/-}$; Smad4$^{-/-}$) were injected in one anterior lobe of a recipient mouse, while the symmetric lobe was injected with saline solution. *n* = 4 for Pten$^{-/-}$-injected mice; *n* = 5 for Pten$^{-/-}$; Smad4$^{-/-}$-injected mice. Student *t* test was performed. *, P < 0.05; ***, P < 0.001 (B, H, and J). SSC-A, side scatter area; SSC-H, side scatter height. Data in B, H, and J are expressed as mean ± SD.

accumulation induces a functional switch in TAMs versus an immunomodulatory phenotype. In summary, mirroring the human PCa findings, we observed infiltration of lipid-loaded TAMs and its correlation with tumor progression and metastatic propensity in murine PCa.

Reciprocal cytokine signaling drives TAM lipid accumulation and PCa cell migration

Increased lipid accumulation in the more aggressive human and murine PCa samples prompted assessment of the role of cancer cells in driving uptake of lipoproteins in bone marrow–derived macrophages (BMDMs) in vitro. To that end, conditioned media (CM) from prostate epithelial cells derived from the various murine PCa models were incubated with BMDMs in the presence of fluorescent PhRodo-neutral (low-density lipoproteins [LDLs]) or Dil-/AF488-modified (oxLDL and acLDL, respectively) lipoproteins (Fig. 5 A). Quantification of lipoprotein uptake by immunofluorescence staining revealed significant uptake of oxLDLs or acLDLs by BMDMs upon exposure to CM from the aggressive Pten$^{-/-}$; Smad4$^{-/-}$ and Pten$^{-/-}$; Trp53$^{-/-}$; Smad4$^{-/-}$; epithelial cells relative to CM from Pten$^{-/-}$ epithelial cells or no-CM controls (Fig. 5, B and C; and Fig. S2 L). Uptake of neutral LDL was not affected by the CM (data not shown). Accordingly, gene expression of *LDLr* was not modulated (Fig. S2 M). BMDMs treated with CM from Pten$^{-/-}$; Smad4$^{-/-}$ cells and Pten$^{-/-}$; Trp53$^{-/-}$; Smad4$^{-/-}$; epithelial cells, but not CM from Pten$^{-/-}$ or untreated control media, increased *Marco* expression (Fig. 5 D), whereas the expression of *Cd36*, known to be involved in lipid uptake by macrophages (Park, 2014), was not altered (Fig. S2 N). To assess the potential role of Marco in the formation of lipid-loaded TAMs, we assessed oxLDL uptake in *Marco* KO BMDMs and observed a significant reduction of oxLDL uptake compared with *Marco* WT controls (Fig. 5, E and F for the Pten$^{-/-}$; Smad4$^{-/-}$ cells; and Fig. S2, O and P for the Pten$^{-/-}$; Trp53$^{-/-}$; Smad4$^{-/-}$ cells). Interestingly, lipid accumulation resulted in an augmented Stat6 activation in macrophages exposed to oxLDL (Fig. S2 Q). Next, to elucidate the cancer cell–derived factors stimulating Marco expression, multiparametric ELISA was used to identify secreted factors that were elevated in the CM Pten$^{-/-}$; Smad4$^{-/-}$ and Pten$^{-/-}$; Trp53$^{-/-}$; Smad4$^{-/-}$; epithelial cells relative to Pten$^{-/-}$ controls. IL-1β, IL-23, and IL-12p40 levels were increased in the aggressive cancer models with IL-1β being the most abundant (Fig. S3, A and B). When tested, recombinant IL-1β produced a dose-dependent increase in *Marco* expression in BMDMs (Fig. S3 C); conversely, anti-IL-1β neutralizing antibody reduced the uptake of oxLDL in BMDMs treated with CM from Pten$^{-/-}$; Smad4$^{-/-}$ cells (Fig. 5 G). Together, these data suggest that cancer cell–derived IL-1β drives *Marco* upregulation, which in turn fosters lipid uptake by macrophages.

Given that lipid-loaded TAMs are a key feature of metastatic PCa and previous studies have shown that TAMs promote cancer cell invasion and metastasis (Lin et al., 2006), we tested the ability of lipid-loaded TAMs to modulate cancer cell migration. To that end, Pten$^{-/-}$; Smad4$^{-/-}$-conditioned BMDMs were incubated overnight with 10 µg/ml oxLDL and then co-cultured with Pten$^{-/-}$; Smad4$^{-/-}$ cancer cells in transwell plates. In this assay, we observed an increased migration of cancer cells upon co-culture with oxLDL-loaded BMDMs relative to normal BMDM or no BMDM controls (Fig. 5 H). Additional assays based on manual counting of migrated cancer cells corroborated these findings (Fig. S3 D). To identify the factors secreted by lipid-loaded macrophages, we performed proteome profiling of Pten$^{-/-}$; Smad4$^{-/-}$ tumor-conditioned macrophages loaded with oxLDL. Among all the factors analyzed, Ccl6 was highly expressed by these tumor-conditioned macrophages and showed further increased expression upon oxLDL exposure (Fig. 5 I). Accordingly, anti-Ccl6 neutralizing antibody treatment of lipid-loaded TAMs resulted in significantly reduced cancer cell migratory capacity compared with control (Fig. 5 J). When analyzed in human PCa TCGA datasets, expression of *CCL23*, the human ortholog of murine *Ccl6*, correlated positively with expression of the pan-macrophage marker *CD68* and with expression of *MARCO* (Fig. S3, E and F). To then provide mechanistic insights into the impact of Ccl6 on tumor invasiveness, we performed a preclinical trial on Pten$^{pc-/-}$; Smad4$^{pc-/-}$ tumor-bearing mice. We administered a neutralizing antibody against Ccl6 (or the isotype as negative control) and analyzed tumors after 14 d of daily injection. Strikingly, Ccl6 neutralization completely hindered tumor invasiveness in treated animals. Tumor size and the composition of the tumor microenvironment were not affected (Fig. S3, G–K). In accordance with our hypothesis on the role of IL-1β on lipid macrophages, *IL-1β* correlates with *CCL23* gene expression in the TCGA cohort (Fig. S3 L). Finally, we also unveiled that Ccr1 gene expression is upregulated in Pten$^{pc-/-}$; Smad4$^{pc-/-}$ metastatic tumors compared with Pten$^{pc-/-}$ organ-confined tumors (Fig. S3 M). In summary, our results indicate that MARCO-dependent lipid uptake on tumor-conditioned macrophages augments the release of Ccl6 which, in turn, fosters cancer cell migration.

Administration of HFD to tumor-bearing mice raises lipid accumulation in TAMs and alters their transcriptional profile

A positive correlation between PCa progression and obesity has been reported, and recent findings showed that exposure to an HFD can impact tumor cell metabolism, resulting in tumor invasiveness and metastasis in PCa mouse models (Chen et al., 2018). TAMs have been reported to play an important role in HFD-induced prostate cancer progression (Hayashi et al., 2018), yet experimental evidence that HFD exerts a direct effect on macrophage lipid metabolism is still lacking. The above findings that cancer cells can foster lipid uptake by TAMs prompted assessment of whether HFD may impact lipid content of infiltrating macrophages in tumor-bearing mice. To this end, PCa cells were injected subcutaneously in NOD-SCIDγ mice, which are defined by lack of B and T cells and altered NK cell activity yet a functional myeloid response. Coincident with tumor onset (10 d after Pten$^{-/-}$; Smad4$^{-/-}$ PCa cell injection), mice were randomly assigned into two experimental groups, the HFD group (45% fat) and the normal-fat diet (NFD; 10% fat) group, and tumor growth was monitored for an additional 25 d (Fig. 6 A). In accordance with epidemiological correlations, tumor growth progressed more rapidly in the HFD group, providing experimental evidence of the role of lipids in driving PCa growth

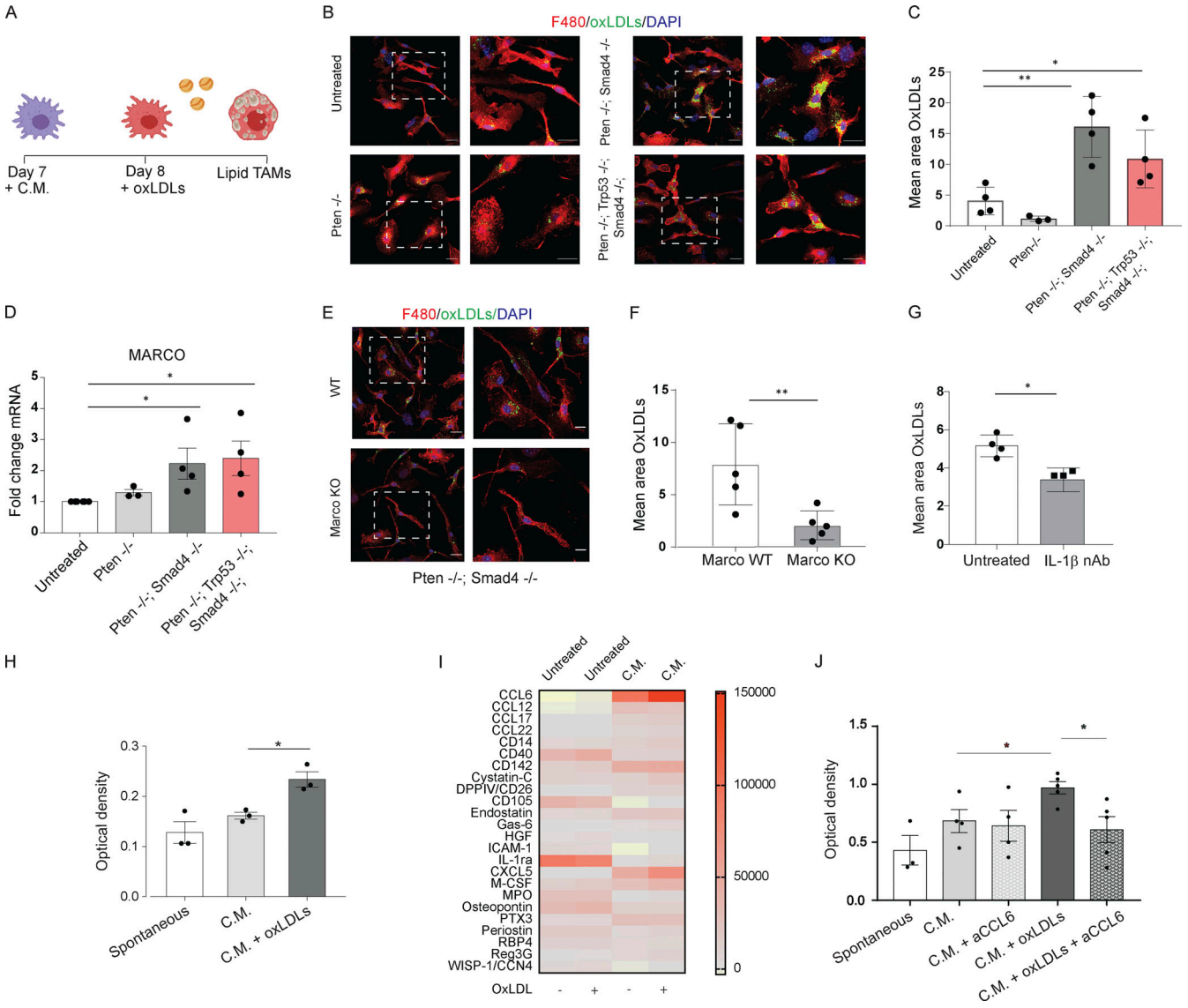

Figure 5. **MARCO-dependent lipid uptake on tumor-conditioned macrophages fosters tumor cell migration by CCL6 release. (A)** Lipid uptake assay scheme and generation of lipid-loaded TAMs. At day 7 of differentiation, primary macrophages were exposed to tumor CM, the day after oxLDLs were added, leading to the formation of lipid-loaded macrophages. **(B and C)** Representative confocal immunofluorescence images and quantification of green-stained oxLDL uptake in red-stained F4/80 stained macrophages exposed to different tumor CM. Nuclei marked with DAPI (blue). Images were acquired with an SP-II confocal microscope (Leica) with a 60× objective. Images on the right are 2× digital zoom. Scale bar, 20 µm (20 µm for digital zoom). *n* = 4 independent experiments for untreated, Pten$^{-/-}$; Smad4$^{-/-}$, and Pten$^{-/-}$; Trp53$^{-/-}$; Smad4$^{-/-}$, and *n* = 3 independent experiments for Pten$^{-/-}$. Mean ± SE areas of oxLDLs per cell are shown. **(D)** Quantitative RT-PCR of MARCO expression in primary macrophages exposed to different tumor CM. FC was calculated on untreated macrophages as control. *n* = 4 independent experiments for untreated, Pten$^{-/-}$; Smad4$^{-/-}$, and Pten$^{-/-}$; Trp53$^{-/-}$; Smad4$^{-/-}$, and *n* = 3 independent experiments for Pten$^{-/-}$. **(E and F)** Representative confocal immunofluorescence images and quantification of green-stained oxLDL uptake in red-stained F4/80 strained MARCO KO and MARCO WT macrophages exposed to Pten$^{-/-}$; Smad4$^{-/-}$ tumor CM. Images were acquired with an SP-II confocal microscope with a 60× objective. Images on the right are 2× digital zoom. *n* = 5. Mean area of oxLDLs per cell ± SE are shown. Scale bar, 20 µm (10 µm for digital zoom). **(G)** Quantification of oxLDL uptake in primary macrophages exposed to Pten$^{-/-}$; Smad4$^{-/-}$ tumor CM and treated with an anti-IL-1β neutralizing antibody (nAb). *n* = 4 for untreated, and *n* = 3 for IL-1β. Mean areas of oxLDLs per cell ± SE are shown. Student's *t* test was performed. **(H)** Migration assay. Pten$^{-/-}$; Smad4$^{-/-}$ tumor cells were indirectly co-cultured in transwell chambers with primary macrophages previously exposed to tumor CM (Pten$^{-/-}$; Smad4$^{-/-}$) and treated or not with oxLDLs (10 µg/ml) for 15 h. Migrated cells on the bottom surface of the membrane were stained with Crystal Violet. Optical density was measured with a CLARIOstar plate reader at 570 λ. Spontaneous migration of Pten$^{-/-}$; Smad4$^{-/-}$ tumor cells was used as baseline. *n* = 3. **(I)** A proteome profiler array was performed on untreated primary macrophages loaded or not with oxLDLs and on primary macrophages exposed to Pten$^{-/-}$; Smad4$^{-/-}$ tumor CM and loaded or not with oxLDLs. Heat map, representative of protein modulation, optical density measurements are shown. Analysis was performed using ImageJ software. **(J)** Migration assay in the presence of anti-CCL6 antibody. Pten$^{-/-}$; Smad4$^{-/-}$ tumor cells were co-cultured in transwell chambers with primary macrophages as described in H. In some conditions, an nAb against CCL6 (15 µl/ml) was added. Spontaneous migration of Pten$^{-/-}$; Smad4$^{-/-}$ tumor cells was used as baseline. *n* = 3 independent experiments were performed and analyzed. Student's *t* test was performed. *, P < 0.05; **, P < 0.01 (C, D, F, and G). Paired Student's *t* test was performed on raw optical density data. *, P < 0.05 (H and J). Data are expressed as mean ± SD.

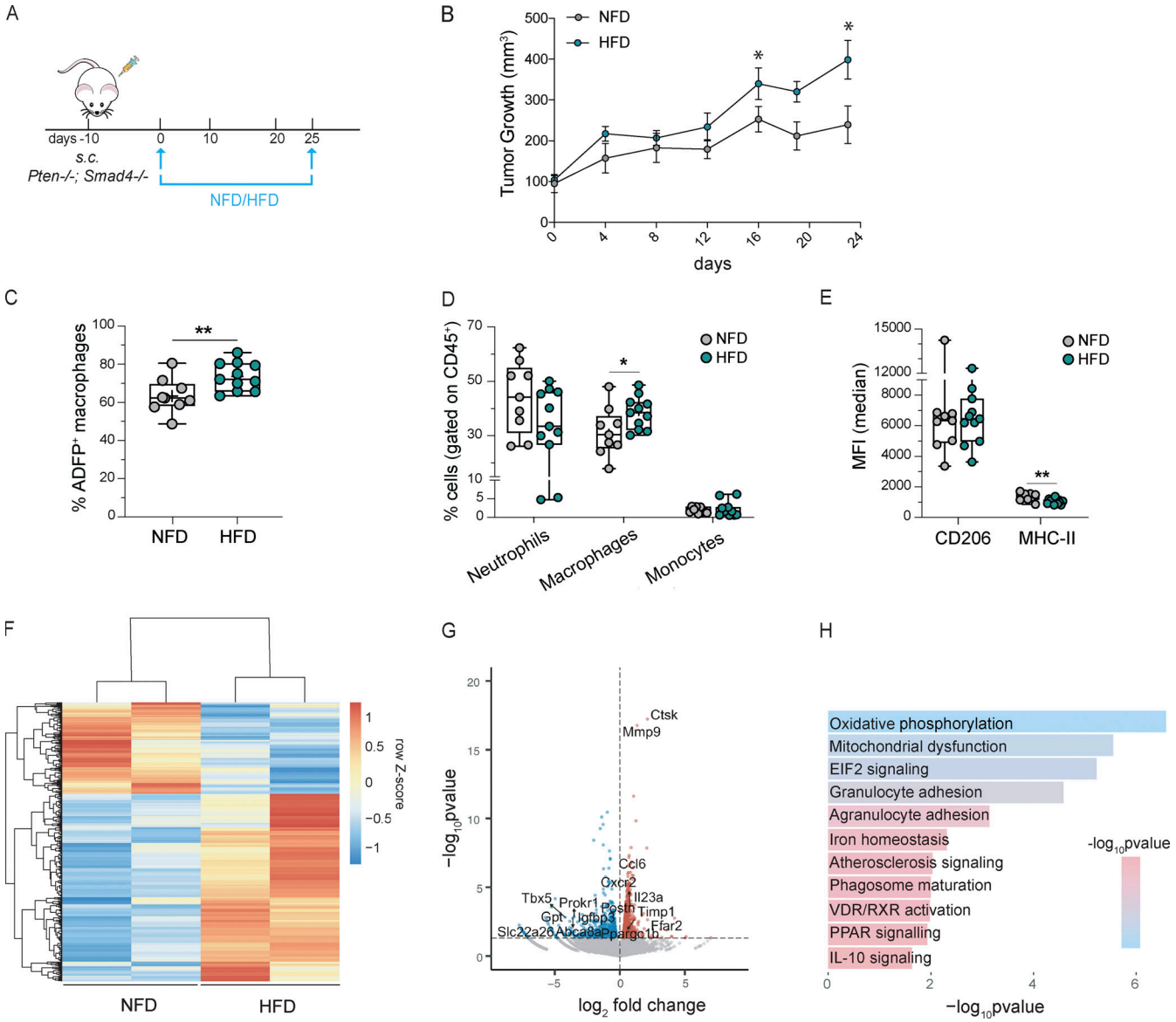

Figure 6. **Administration of an HFD to tumor-bearing mice raises lipid accumulation in TAMs and alters their transcriptional profile. (A)** Scheme of HFD effects on tumor growth and TAM phenotype experiments. NOD-SCIDγ mice were injected subcutaneously with Pten$^{-/-}$; Smad4$^{-/-}$ cells. After 10 d, tumors were clearly visible on the flanks, and mice were randomized into two treatment groups: HFD (n = 11) and NFD (n = 9). **(B)** Tumor growth in NOD-SCIDγ mice injected subcutaneously with Pten$^{-/-}$; Smad4$^{-/-}$ cells fed NFD or HFD. Measurements began 10 d after the initial cell injection. **(C)** Characterization of the immune infiltrate in subcutaneous Pten$^{-/-}$; Smad4$^{-/-}$ tumors in NOD-SCIDγ mice fed either with NFD or HFD. **(D)** Percentage of ADFP^{+} macrophages in tumors from NOD-SCIDγ mice injected subcutaneously with Pten$^{-/-}$; Smad4$^{-/-}$ cells and fed either NFD or HFD. **(E)** Phenotypic characterization of tumor-infiltrating TAMs in subcutaneous Pten$^{-/-}$; Smad4$^{-/-}$ tumors in NOD-SCIDγ mice fed either with NFD or HFD. **(F)** RNA-seq analysis performed on TAMs (CD45^{+}F4/80^{+}Ly6G^{-}) isolated from Pten$^{-/-}$; Smad4$^{-/-}$ tumors in NOD-SCIDγ mice. Heat map shows normalized gene expression values of significantly modulated genes in HFD- versus NFD-fed mice. **(G)** Volcano plot showing differentially expressed genes according to their P value. Modulated genes are colored according to their log$_2$FCthresholds. **(H)** IPA of differentially expressed genes. Significant canonical pathways are represented according to their −log$_{10}$ P value. Student's t test was performed (B–E). *, P < 0.05; **, P < 0.01. MFI, mean fluorescence intensity. Data in C–E are expressed as mean ± SD.

(Fig. 6 B). FACS analysis of treated mice revealed a significant increase of ADFP^{+} macrophages (lipid-loaded TAMs) in HFD-fed mice relative to NFD controls (Fig. 6 C). Interestingly, the percentage of ADFP^{+} DCs was augmented upon HFD exposure, while monocytes and neutrophils were not affected (Fig. S4 A), indicating that diet exposure may have a broad effect on the tumor immune infiltrate. Furthermore, flow cytometry profiling of myeloid subsets in tumors showed a perturbation of the macrophage compartment in HFD-fed mice, as evidenced by a significant increase in the percentage of macrophages (Fig. 6 D) and a decrease in MHC-II expression on macrophages, a finding suggestive of altered macrophage activation (Fig. 6 E). Next, RNA-seq was performed on sorted tumor-infiltrating CD45^{+}CD11b^{+}F4/80^{+}Ly6G^{-} macrophages from NFD- and HFD-fed mice, documenting altered transcriptional profiles of the macrophages from the tumors of HFD and NFD mice (n = 551

genes; P < 0.01; Fig. 6 F). In the HFD samples, the most significant genes were those known to be involved in the protumor activity of TAMs (*cathepsin K*, *Mmp9*, *IL-23a*, *Cxcr2*) and regulators of lipid metabolism (*Fabp5*). Moreover, *Ccl6* was significantly increased in HFD-sorted macrophages in accordance with in vitro data (Fig. 6 G). IPA of differentially expressed genes highlighted the upregulation of terms associated with mitochondrial function (oxidative phosphorylation), lipid metabolism (atherosclerosis signaling, PPAR signaling), and immunomodulation (EIF2 signaling, granulocyte adhesion and diapedesis, IL-10 signaling; Fig. 6 H). Finally, GSEA revealed the activation of the Stat6-dependent pathway in TAMs from the HFD mice, in accordance with in vitro data showing Stat6 activation upon lipid loading (Fig. S4 B). Together, these results indicate that HFD can raise the abundance of lipid-loaded TAMs in PCa and alter the transcriptional and secretory profile of TAMs.

Marco blockade impairs lipid loading in TAMs and hinders tumor growth and invasiveness

The role of Marco in modulating lipid accumulation in macrophages and consequent cancer cell migratory activity encouraged assessment of the impact of αMarco neutralizing antibody on tumor progression in the Pten$^{pc-/-}$; Smad4$^{pc-/-}$ model. αMarco treatment was initiated at 9 wk of age, coinciding with the time of tumor initiation, and continued for an additional 14 d (Fig. 7 A). αMarco treatment resulted in a significant reduction in tumor volume relative to control (Fig. 7 B). Pathological analyses revealed 25% invasive tumors in the αMarco treatment group versus 80% invasive tumors in the control group (Fig. 7 C). FACS analysis showed decreased frequency of lipid-loaded ADFP$^+$F4/80$^+$ macrophages in the αMarco treatment group relative to the control group (Fig. 7 D), which was confirmed by immunofluorescence analysis of tumor sections (Fig. 7 E). This analysis also identified alterations in the macrophage compartment of αMarco-treated tumors, characterized by a decreased frequency of macrophages and an upregulation of MHC-II expression, consistent with reprogramming toward a proinflammatory functional state (Fig. 7 F and Fig. S4, C and D). Of note, in these settings, there were no changes in CD36 expression, as described previously to be involved in the regulation of lipid metabolism in TAMs (Fig. S4 D). The adaptive immune compartment did not exhibit changes in cell abundance, including CD4$^+$ and CD8$^+$ T cells, Treg cells (CD4$^+$/CD25$^+$ cells), and double-negative unconventional T cells (Fig. S4 E) in agreement with previous reports (Georgoudaki et al., 2016). Finally, the αMarco treatment group showed a significant increase in the percentage of cytotoxic CD11b$^+$ NK cells indicative of increased NK cell activation/maturation, which raised the possibility that NK cells may contribute to the antitumor activity of the αMarco antibody treatment (Fig. 7 G).

To show more directly that Marco-expressing TAMs play a key role in the antitumor effects of the αMarco antibody, treatments were tested in NOD-SCIDγ mice, which lack the adaptive immune response and show a defective NK cell compartment. 10 d after subcutaneous injection of Pten$^{-/-}$; Smad4$^{-/-}$ PCa cancer cells in NOD-SCIDγ mice, αMarco antibody was administered intravenously. We observed a significant reduction in tumor volume in αMarco antibody–treated mice relative to isotype controls, which showed continued tumor growth (Fig. S4 F). FACS analysis and immunofluorescence staining confirmed a significant reduction in the frequency of lipid-loaded TAMs and ADFP staining documented in the αMarco antibody–treated tumors (Fig. S4 G) and a correlation between Marco and lipid content (Fig. S4, H–K). To also investigate the impact of Marco on lipid uptake upon HFD feeding, we tested Marco neutralization in Pten$^{-/-}$; Smad4$^{-/-}$ tumor-bearing mice exposed to HFD. Mice were exposed to HFD or chow diet as control and were administered with αMarco antibody for 15 d (Fig. S5 A). Strikingly, Marco neutralization resulted in inhibition of tumor growth in HFD-treated mice (Fig. S5 B). Importantly the frequency of ADFP$^+$ macrophages, among total CD11b$^+$F4/80$^+$LY6G$^-$ macrophages was significantly reduced by Marco blockade (Fig. S5 C). The relative abundance of macrophages and neutrophils was not affected (Fig. S5, D and E). In addition, signaling pathways related to IL-1β release were significantly enriched in tumor epithelial cells isolated from HFD-treated mice compared with NFD mice, suggesting that IL-1β may be implicated in the observed phenotype (Fig. S5, F and G). Altogether, these results support the hypothesis that Marco, at least partially, mediates lipid intake in TAMs upon HFD exposure.

TAMs have been previously reported to contribute to treatment failure in advanced PCa, and depletion of TAMs has been described to increase response to docetaxel in this context (Escamilla et al., 2015; Guan et al., 2019). In addition, aberrant lipid metabolism has been associated with resistance to certain antitumor therapies (Bacci et al., 2021). This evidence encouraged us to investigate whether lipid accumulation in TAMs may contribute to chemotherapy resistance in prostate cancer. To this end, PCa cells were injected subcutaneously in NOD-SCIDγ mice exposed to docetaxel in the presence or absence of αMarco administration (Fig. 7 H). As expected, tumor growth was partially delayed upon both docetaxel and αMarco administration relative to untreated controls (Fig. 7, I and J, with 7 J showing day 14 of treatment). Importantly, the combinatorial approach based on docetaxel and αMarco further suppressed tumor growth (Fig. 7, I and J, with 7 J showing day 14 of treatment). We observed that docetaxel administration was associated with an increased frequency of TAMs and a significant upregulation of CD206 on infiltrating macrophages. CD206 upregulation may be indicative of a protumor activation state of TAMs. Importantly, these effects were reverted when αMarco was administered in combination with docetaxel (Fig. 7, K and L). FACS analysis of treated mice also revealed a significant decrease of ADFP expression in macrophages in mice treated with the combinatorial approach, relative to control, that was not observed in the presence of docetaxel alone (Fig. S5 H). Importantly, the decrease in lipid loading may be responsible for macrophage reprogramming in the combinatorial approach. Finally, lipid-loaded macrophages were shown to decrease the percentage of annexin$^+$ tumor cells exposed to docetaxel in vitro, indicating that lipid-loaded TAMs may support resistance of cancer cells to the proapoptotic activity of taxanes (Fig. S5 I). Collectively, these data indicate that Marco blockade drives a reduction of lipid content in tumor-infiltrating

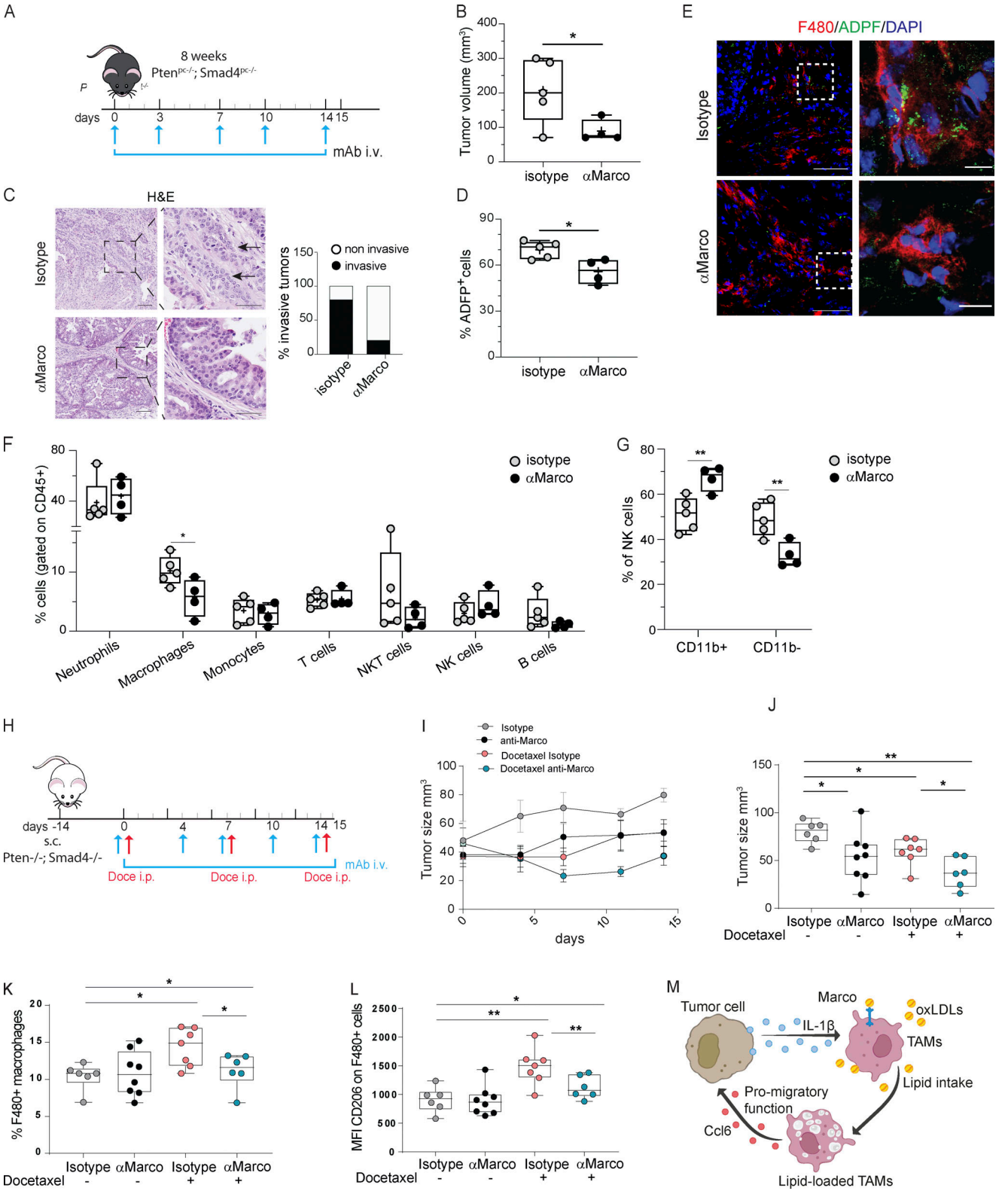

Figure 7. **MARCO blockade in prostate tumor models impairs lipid-loading in TAMs and hinders tumor growth and invasiveness. (A)** Scheme of αMarco treatment in Pten$^{pc-/-}$; Smad4$^{pc-/-}$ mice. Mice at 9 wk of age were either treated with αMarco antibody or with an isotype control (100 µg/injection on days 0 and 3 and 50 µg/injection on days 7, 10, and 14). *n* = 4 mice treated with αMarco, and *n* = 5 mice treated with isotype control. Mice were sacrificed at day 15. **(B)** Tumor size in Pten$^{pc-/-}$; Smad4$^{pc-/-}$ mice treated with αMarco antibody or control isotype. Measures were taken on the day of sacrifice. **(C)** Representative images of H&E staining of anterior prostate lobes from Pten$^{pc-/-}$; Smad4$^{pc-/-}$ mice treated with αMarco or isotype control. Arrows indicate invasive areas. Images were acquired with a VS120 dotSlide Microscope (Olympus) with a 20× objective. Scale bar, 100 µm (50 µm for digital zoom). **(D)** Percentage of ADFP^{+} macrophages in tumors from Pten$^{pc-/-}$; Smad4$^{pc-/-}$ mice treated with αMarco antibody or isotype control. **(E)** Representative confocal

immunofluorescence images of tumor anterior prostate lobes from Pten$^{pc-/-}$; Smad4$^{pc-/-}$ mice treated with αMarco or control isotype. Red-stained F4/80$^+$ macrophages colocalize with green-stained ADFP lipid droplets in the isotype control group versus the αMarco-treated group. Images were acquired with an SP8-II confocal microscope (Leica) with a 40× objective. Images on the right are 2× digital zoom. Scale bar, 50 µm (10 µm for digital zoom). **(F)** Expression of macrophage markers by TAMs from Pten$^{pc-/-}$; Smad4$^{pc-/-}$ tumors from mice treated with αMarco or with isotype control. *n* = 4 for αMarco, and *n* = 5 for isotype control. **(G)** Frequency of NK cells in Pten$^{pc-/-}$; Smad4$^{pc-/-}$ tumors from mice treated with αMarco or with isotype control. Cytotoxic NK cells were identified as CD11b$^+$. **(H)** Scheme of αMarco/docetaxel treatment in NOD-SCIDγ mice injected subcutaneously with Pten$^{-/-}$; Smad4$^{-/-}$ cells. After 10 d, tumors were clearly visible on the flanks, and mice were randomized into treatment groups. *n* = 8 for αMarco, *n* = 7 for isotype control, *n* = 7 for docetaxel plus isotype control, and *n* = 6 for docetaxel plus αMarco. **(I)** Graph showing the growth curves of tumors. Ordinary one-way ANOVA of curves. P = 0.004. Areas under the curves are as follows: control = 923.5; αMarco = 648.2, docetaxel = 594.9, docetaxel + αMarco = 445.8. **(J)** Bar graph showing tumor growth in NOD-SCIDγ mice injected subcutaneously with Pten$^{-/-}$; Smad4$^{-/-}$ cells and treated with αMarco/docetaxel. **(K and L)** Bar graph showing the percentage of F4/80$^+$ macrophages (gated on CD11b$^+$) and the median fluorescence intensity (MFI) of CD206 on macrophages in tumors from NOD-SCIDγ mice injected subcutaneously with Pten$^{-/-}$; Smad4$^{-/-}$ cells and treated with αMarco/docetaxel. **(M)** Scheme of the mechanism of induction and of lipid-loaded TAMs and their function. Student's *t* test was performed (B, D, F, G, and J–L). *, P < 0.05; **, P < 0.01. Doce, docetaxel. Data in B, D, F, G, and J–L are expressed as mean ± SD.

macrophages, impairs tumor growth and invasiveness, and improves response to chemotherapy in PCa models (Fig. 7 M).

Discussion

While TAMs can drive tumor progression and poor clinical outcome in human PCa (Cao et al., 2017; Di Mitri et al., 2019), the complexity and functional diversity of macrophage populations have hampered the development of effective therapeutic strategies. Here, we focused on the single-cell profiling of CD45$^+$ tumor-infiltrating leukocytes from aggressive human PCa and the integration of such data with transcriptomic profiles of murine PCa models of varying aggressiveness. High-dimensional single-cell profiling identified a subset of MARCO-expressing TAMs characterized by altered transcriptional pathways associated with lipid metabolism and accumulation of lipids. The frequency of lipid-loaded TAMs correlated positively with tumor progression in men and mouse models of PCa. Mechanistically, IL-1β secreted by PCa cells upregulates Marco expression to drive lipid loading; conversely, lipid-loaded TAMs secrete Ccl6 to drive PCa cell migration. Correspondingly, Marco neutralization reduces the abundance of lipid-loaded TAMs and hinders tumor progression, revealing a novel therapeutic target for advanced PCa.

The identification of prognostic determinations for men presenting with PCa has been challenged by significant intratumor heterogeneity on the cellular and molecular levels (Sebastian de Bono et al., 2011). Previous work integrating mouse and human data has resulted in the identification of signatures with clinical utility in assigning risk of disease progression and lethality (Dow et al., 2018; Zilionis et al., 2019). To more precisely identify the cellular and molecular drivers of PCa aggressiveness, we combined the strategies of single-cell analysis and cross-species comparisons to develop a prognostic gene signature based on the MARCO-expressing TAM transcriptome. That said, we acknowledge that further study will be necessary to evaluate the utility of this transcriptome in predicting clinical outcomes. Moreover, it is important to note that such signatures are derived from a specific cancer genotype (i.e., expression of both *MARCO* and our signature was enriched in *PTEN*-deleted tumors but not in *TRP53*- and *RB1*-deleted tumors), thus denoting that tumor genotype may influence the functional phenotype of TAMs. This is in accordance with previous findings showing that the genetic alteration in prostate cancer drives the tumor immune landscape (Bezzi et al., 2018; Wang et al., 2016). We speculate that both genotype and immune profiles will be critical in building models for risk stratification as well as for the identification and application of targeted therapies for specific PCa patient populations.

Additionally, we reported that lipid loading confers protumorigenic functions to macrophages, as it enhances their ability to increase tumor cell migration driven by Ccl6. Of note, a recent report showed that Ccl8 released by TAMs is prognostic of poor survival in breast cancer, further supporting the role of chemokines in mediating the protumor activity exerted by TAMs and revealing that the specific TAM secretome can depend on tumor type. In accordance with our in vitro data, Marco neutralization in vivo hinders lipid accumulation by TAMs and reprograms macrophages, inhibits tumor growth, and reduces cancer invasion in immunocompetent mice. Notably, we confirmed the same results in NOD-SCIDγ mice, which lack T, B, and NK cell–mediated responses, thus indicating that macrophages are a key target for antitumor activity of Marco blockade. Our observations align with previous findings that Marco blockade affects macrophage polarization in subcutaneous mouse models of colon cancer and melanoma (Georgoudaki et al., 2016). Finally, MARCO-expressing TAMs have been identified in diverse human cancers, including hepatocellular carcinoma and lung adenocarcinoma (Lavin et al., 2017; Zhang et al., 2019), raising the possibility that MARCO blockade may have broader therapeutic relevance in multiple tumor types. Interestingly, in our in vivo models, Marco neutralization resulted in reduction of total macrophages infiltrating the tumors. This evidence suggests that the ED31 αMarco antibody partially induces macrophage depletion, a possibility that should be further investigated.

Lipid metabolism has been extensively explored in cancer, and a large body of evidence supports the concept that intrinsic lipogenesis in tumor cells and exposure to an HFD promote tumor progression and metastasis (Dang et al., 2019; Stoykova and Schlaepfer, 2019). Numerous studies reported the association between dyslipidemia and PCa, and our experimental findings align with previous evidence showing that higher levels of plasma LDLs and oxLDLs correlate positively with increased Gleason score (data not shown; Wan et al., 2015). Moreover, exposure to an HFD was reported to drive metastasis in a mouse model of PCa upon lipid accumulation in cancer cells (Chen et al., 2018). Our work provides evidence that exposure to

HFD drives a dysregulation in lipid-associated transcriptional pathways in TAMs, alters TAMs lipid content, and downregulates MHC-II. These results raise the possibility that exposure to dietary lipids can directly affect the function of TAMs, including modulation of their secretome, thus enabling TAMs with protumorigenic functions. Thus, our findings sustain the rationale of targeting lipid metabolism in the tumor microenvironment (Baenke et al., 2013; Peck and Schulze, 2019) and support the importance of incorporating a dietary regimen in the therapeutic strategies in PCa. Interestingly, the uptake of cholesterol mediated by scavenger receptors expressed on cancer cells has been linked to cancer aggressiveness in castration-resistant prostate cancer (González-Chavarria et al., 2014; Gordon et al., 2019). Here, we unveiled a connection between the expression of the scavenger receptor MARCO and the accumulation of lipid droplets in TAMs that was previously uncovered. Our results extend the concept of lipid loading mediated by cell scavenging to the tumor microenvironment and implicate that scavenger receptors may be a valuable therapeutic option in PCa. Importantly, lipid metabolic reprogramming in cancer cells has been associated with failure of antitumor therapies. Still, the mechanisms by which the accumulation of lipids in the tumor microenvironment affects therapy response are still unresolved. Here, we support the concept that a dysregulation in lipid metabolism in tumor-infiltrating macrophages drives resistance to chemotherapy. It will be important to understand how lipid-loaded macrophages hinder the efficacy of docetaxel in !advanced PCa. This notion may support the development of combinatorial therapies that target lipid-loaded macrophages or the accumulation of lipids in the tumor immune microenvironment with chemotherapy.

In conclusion, our findings provide insights into the role of TAMs in PCa and reveal novel therapeutic targets and strategies for enhancement of an innate-driven antitumor response. Consistent with prior studies in colon carcinoma and melanoma (Georgoudaki et al., 2016), our work encourages the application of MARCO blockade as a strategy to improve the effectiveness of therapies targeting the adaptive branch of the immune response, which to date has shown meager clinical benefit in PCa. Indeed, the concept of targeting the myeloid lineage in PCa has shown promise in mouse models of metastatic castration-resistant PCa where inhibition of myeloid-derived suppressor cells, together with immune checkpoint blockade therapy, has elicited tumor eradication (Lu et al., 2017). Our work expands this concept and further sustains the evidence that TAMs may be a therapeutic target in PCa (Di Mitri et al., 2019). For this reason, combinatorial approaches targeting both the adaptive and the innate branches of the immune response should be evaluated further in the clinical setting.

Materials and methods

Human samples

Patients affected by PCa were enrolled at Humanitas Clinical and Research Centre, Rozzano, Milan, Italy. Patients were treatment naive at the time of analysis. All patients provided written informed consent in accordance with the Declaration of Helsinki. The protocol was approved by the Ethical Committee of Humanitas Clinical and Research Hospital.

scRNA-seq processing

Human prostatic tumor and nontumor tissues were dissociated to single-cell suspension. Briefly, tumors were digested for 1.5 h in a collagenase type V solution (0.5 mg/ml) at 37°C in 5% CO_2 on a rocking platform. Cell digestion was then pelleted and incubated in 2.5% trypsin for 5 min at 37°C in 5% CO_2. Trypsin was then inactivated by complete medium with FBS, and cell suspension was further passed through a syringe needle until complete dissociation and filtered through a 40-µm cell strainer. $CD45^+$ cells were sorted by flow cytometry, resuspended in 1 ml PBS plus 0.04% BSA, and washed two times by centrifugation at 450 rcf for 7 min. After the second wash, cells were resuspended in 30 µl and counted with an automatic cell counter (Countess II; Thermo Fisher Scientific) to get a precise estimation of total number of cells recovered. Afterward, $CD45^+$ cells of each sample were loaded into one channel of the Single Cell Chip A using the Single Cell 3′ v2 Reagent Kit (10X Genomics) for generation of gel bead emulsion into the Chromium system. Following capture and lysis, cDNA was synthesized and amplified for 14 cycles according to the manufacturer's protocol (10X Genomics). 50 ng of the amplified cDNA was then used for each sample to construct Illumina sequencing libraries. Sequencing was performed on the Illumina NextSeq 500 sequencing platform following 10X Genomics instruction for reads generation. A sequencing depth of at least 20,000 reads/cell was obtained for each sample.

scRNA-seq analysis

Unsupervised clustering analysis

Raw sequencing data in the format of BCL files were converted in FASTQ files and aligned to the human reference genome GRCh38, taking advantage of the Cell Ranger Pipeline (version 3.0.2) provided by 10X Genomics. After quality check, we obtained 6,362 and 10,951 cells, respectively, for normal and tumor tissue. Filtered gene expression matrices from Cell Ranger were used as input for clustering analysis by Seurat R package (version 3.0.2; R version 3.5.1; Stuart et al., 2019). We first processed each individual dataset separately, considering the thresholds of 200, 20,000, and 0.2 respectively for number of genes, number of unique molecular identifiers, and mitochondrial content. For each dataset, we selected the top 2,000 most variable genes. Subsequently, we used the FindIntegrationAnchors function to combine the datasets together, choosing 2,000 anchor genes for integration. After integration, we ran a principal component analysis and selected the first 20 principal components to perform Louvain clustering and uniform manifold approximation and projection embedding. Finally, we obtained a total of 18 clusters (resolution level = 0.6). Differential expression analyses were performed through the FindMarkers function, applying the Wilcox test by default (adjusted $P < 0.05$). Reclustering of macrophage clusters was performed by subsets of cells belonging to Cl2, Cl9, and Cl11 for both conditions (normal and tumor tissue). For the integrated analysis (normal and tumor tissue), 2,494 cells were selected and clustered using the first 30 principal components and a resolution level of 0.5, giving rise to eight clusters. For tumor tissue, 1,704 cells were considered for the analysis. The clustering was performed choosing the first 16

principal components and a resolution of 0.5, producing a total of seven clusters. To assign clusters to cell types, we used SingleR algorithm (version 1.2.4; Aran et al., 2019), applying a fine-tuning step and the Novershtern hematopoietic cell data as the reference dataset (Novershtern et al., 2011).

Functional trajectory inference

Monocle3 (version 0.2.0; R version 3.6.1) was used to identify functional trajectory, ordering transcriptome profiles of single cells in an unsupervised manner without a priori knowledge of marker genes (Trapnell et al., 2014). Seurat objects were used as input for pseudotime inference, and the total gene expression matrix was used as reference. Cells were assigned to partitions, and the learn_graph() function was used to fit a principal graph within each partition. Root starting node was automatically assigned and visually inspected by graphical interface. Genes differentially expressed on the different paths through the trajectory were selected (adjusted $P < 0.05$), and cells were ordered along the trajectory according to their pseudotime values. Finally, trajectory-variable genes were collected into modules to define coregulated elements (resolution set to $1e^{-2}$).

Derivation of Mac2-specific gene signature

Reclustering of tumor cells belonging to Cl2, Cl9, and Cl11 was used as input for gene signature derivation. To identify marker genes, we performed a differential expression analysis (Wilcox test) between cluster 1 (identified as MARCO_Mac cluster) and the remaining clusters, excluding the contaminated T cells cluster. Significantly upregulated genes (adjusted $P < 0.05$ and average $\log_2FC > 0$) were analyzed by IPA (Canonical Pathways Analysis). Genes annotated in significant pathways ($-\log_{10} P > 1.3$) related lo lipid metabolism were considered for gene signature definition. The resulting gene signature comprised nine genes (*APOC1*, *CCL2*, *MMP9*, *MARCO*, *FN1*, *FBP1*, *FABP5*, *CTSD*, and *CTSL*) that were strongly upregulated in our cluster (average $\log_2FC > 1$). We manually added *CD68* as a lineage-specific marker gene. Violin plots of gene signature enrichment along clusters were performed by applying the AddModuleScore Seurat function.

Functional analysis of differentially expressed genes

Functional enrichment of differentially expressed genes was performed using IPA (QIAGEN). Pathways belonging to the Canonical Pathway Analysis section were considered for the analysis ($-\log_{10}$ P value > 1.3). For Amit gene signature (Jaitin et al., 2019), we used the GSEA tool through the GSEAPreranked function, using the classic enrichment statistics and meandiv as normalization mode (Subramanian et al., 2005). The complete list of differentially expressed genes in Cl11 with respect to the other clusters was used to assess the enrichment.

Public gene expression dataset analysis

The Prostate Adenocarcinoma and Taylor datasets were used to evaluate the prognostic performance of the gene signature derived from MARCO_Mac cluster. For TCGA, gene expression data (as fragments per kilobase of transcript per million mapped reads [FPKM] values), genomic data (as copy number alterations), and clinical data were downloaded from University of California, Santa Cruz, Xena (http://xena.ucsc.edu). The Taylor dataset was downloaded from Gene Expression Omnibus under accession no. GSE21034 (Taylor et al., 2010), and gene expression values were used as robust multiarray average normalized values. For both datasets, the mean expression value of the gene signature was considered as a normalized *z* score, in which each gene was normalized according to its mean and SD among all patients. Scatter plots of gene expression correlation were performed using the ggscatter function implemented in the ggpubr R package (version 0.3.0), using Pearson's correlation as the statistical method. Prognosis correlation (DFS) was performed on the Prostate Adenocarcinoma dataset using the GEPIA2 tool (http://gepia2.cancer-pku.cn; Tang et al., 2019).

3′-mRNA-seq processing

RNA quality control was performed with the Agilent 2200 TapeStation system, and only RNAs having an RNA integrity number >8 were used for library preparation. Libraries for mRNA-seq were prepared starting from 5 ng total RNA for each sample by using the SMART-Seq v4 Ultra Low Input RNA Kit (Clontech–Takara). Libraries were obtained and qualitatively assessed by using the Agilent 4200 TapeStation and quantified by Qubit Fluorimeter. All samples were sequenced on an Illumina NextSeq 500 at an average of 40 million 75-bp single-end reads.

Total RNA-seq processing

Total RNA-seq library preparation was performed starting from 0.5 ng of total RNA with the SMART-Seq Stranded Kit (Clontech–Takara). Libraries were obtained and qualitatively assessed by using the Agilent 4200 TapeStation and quantified by Qubit Fluorimeter. Afterward, they were multiplexed in an equimolar pool and sequenced on an Illumina NextSeq 500 Platform, generating at least 40 million 75-bp–PE reads per sample (i.e., 80 million reads/sample).

RNA-seq analysis

Raw reads were preprocessed for adapter trimming, and quality check was assessed using the FastQC tool (http://www.bioinformatics.babraham.ac.uk/projects/fastqc). Reads were aligned to the reference genome (Ensembl *Mus musculus* release GRCm38) using the STAR algorithm (version 020201; Dobin et al., 2013). The featureCounts package (version 1.6.4) implemented in the Rsubread package was used to estimate read counts along genes. Differential expression analysis was performed using the GLM approach implemented in the R/Bioconductor edgeR (Robinson and Oshlack, 2010) package (edgeR version 3.24.3; R version 3.5). The resulting differentially expressed genes were analyzed using IPA.

Cell culture

The $Pten^{-/-}$; $Smad4^{-/-}$ and $Pten^{-/-}$; $Trp53^{-/-}$; $Smad4^{-/-}$ prostatic tumor cell lines were provided by R.A. DePinho. The $Pten^{-/-}$ cells are homozygous for Pten deletion and were generated from mouse tissue that had not been subjected to hormone ablation therapy and are thus ideal for the study of human refractory PCa

formation, with tumor growth limited to the prostate gland. The Pten$^{-/-}$; Smad4$^{-/-}$ and Pten$^{-/-}$; Trp53$^{-/-}$; Smad4$^{-/-}$ cells derive from murine tumors that acquire a more aggressive and invasive phenotype. Cells were grown in complete medium comprising DMEM with high glucose (4,500 mg/liter; Sigma-Aldrich) supplemented with 10% heat-inactivated FBS (Sigma-Aldrich), penicillin/streptomycin solution (penicillin G 10 U/ml + streptomycin 0.1 mg/ml; Euroclone), 2 mM L-glutamine (Euroclone), and 1 mM sodium pyruvate solution (Euroclone) at 37°C in 5% CO_2. The Pten$^{-/-}$ prostatic tumor cells were cultured in the same conditions; however, 25 µg/ml bovine pituitary extract (Gibco BRL, Invitrogen), 5 µg/ml human recombinant insulin, and 6 ng/ml human recombinant human epidermal growth factor (PeproTech) were added to the complete medium. CM from prostatic tumor cell lines were collected after 48 h growth in complete medium. For the production of CM derived from Pten$^{-/-}$ prostatic cells line, no additional factors were added to the complete medium.

In vitro differentiation of BMDMs

BMDMs were differentiated in vitro. Briefly, bone marrow precursors were flushed from long bones of C57BL/6N mice or MARCO KO/WT mice and cultured in DMEM high glucose supplemented with 10% heat-inactivated North American FBS in the presence of 20 ng/ml M-CSF (PeproTech) for 7 d. At day 4, half of the medium was replaced with fresh medium, and an additional 20 ng/ml M-CSF was added. On day 7, media were replaced by CM diluted 1:1 in complete medium. For IL-1β stimulation, 5 × 10^5 primary macrophages were plated in two six-well plates and then exposed to 100, 50, and 10 ng/ml IL-1β (PeproTech) for 48 h.

RT-PCR

RNA was isolated by TRIzol reagent (Thermo Fisher Scientific) and reverse transcribed using High-Capacity RNA-to-cDNA Kit (Applied Biosystem) according to the manufacturer's instructions. Quantitative RT-PCR reactions (Applied Biosystem) for each sample were done in triplicate using Fast SYBR Green (Applied Biosystems) and run on the Applied Biosystem QuantStudio 7 Flex Real-Time PCR System. Melting curves were analyzed to confirm the amplification specificity. Relative quantifications of gene expression were done according to the ΔΔCT method. Student's *t* test was performed based on ΔCTs. GAPDH was used as the reference gene. The primer sequences were obtained from PrimerBank and were the following: MARCO forward 5′-AGAGGGAGAGCACTTAGCAG-3′, reverse 5′-CTGTGCCCCGACAATTCACAT-3′; CD36 forward 5′-ATGGGC TGTGATCGGAACTG-3′, reverse 5′-GTCTTCCCAATAAGCATG TCTCC-3′; GAPDH forward 5′-AGGTCGGTGTGAACGGATTTG-3′, reverse 5′-TGTAGACCATGTAGTTGAGGT-3′.

Lipid uptake assay

Lipid uptake assays were performed using neutral LDLs, acLDLs, or oxLDLs conjugated with different fluorophores (Alexa Fluor 488 for neutral LDLs and acLDLs or Dil for oxLDLs; Thermo Fisher Scientific). Briefly, BMDMs were plated on sterile glass coverslips and exposed for 48 h to Pten$^{-/-}$, Pten$^{-/-}$; Smad4$^{-/-}$, and Pten$^{-/-}$; Trp53$^{-/-}$; Smad4$^{-/-}$ tumor CM diluted 1:1 in complete medium and then replaced with serum-free complete medium containing 2.5 µg/ml Alexa Fluor 488–conjugated neutral LDLs, acLDL, or Dil-conjugated oxLDL overnight. The internal control received stimuli with modified LDL but was previously exposed for 48 h to complete medium instead of CM. After 24 h incubation, the media were removed, and immunofluorescence staining was performed. When imaging was not required, lipid uptake assays were performed using unconjugated oxLDLs (Thermo Fisher Scientific) with the same protocol. For IL-1β neutralizing experiments, the same protocol was applied; however, an anti-IL-1β antibody was added in the appropriate wells (150 ng/ml).

Proteome

To analyze the proteome of primary macrophages exposed to tumor CM and modified lipoproteins, we used Proteome Profiler Mouse XL Cytokine Array (R&D Systems), and data were analyzed using ImageJ software according to the manufacturer's instructions.

Multiplex ELISA on tumor CM

The CM of each prostatic tumor cell line was concentrated 1:5 in Amicon Ultra Centrifugal Filter Units (30-kD filter; Sigma-Aldrich), and then a multiplex ELISA analyzing 42 different cytokines (Proteome Rodent MAP 4.0; Myriad) was performed.

Migration assay

2 × 10^5 BMDMs were plated in a 24-well plate and then incubated in Pten$^{-/-}$; Smad4$^{-/-}$ CM for 48 h followed by overnight incubation in serum-free DMEM with 10 µg/ml oxLDL. Subsequently, 3 × 10^4 Pten$^{-/-}$; Smad4$^{-/-}$ tumor cells were plated on the upper chamber of 0.8-µm transwell inserts, which were then placed in the 24-well plates where macrophages had been previously grown. Tumor cells co-cultured with tumor-conditioned macrophages that were not exposed to oxLDLs were used as a control. Tumor cells alone were used to evaluate basal migration. After 15 h, indirect co-culture was stopped. The unmigrated cells on the top side of the membrane were removed. Membranes were then cut and fixed in 4% paraformaldehyde (PFA) followed by 0.5% Crystal Violet (Sigma-Aldrich) staining for 20 min on a shaker. Membranes were left to dry overnight, and Crystal Violet was extracted using 20% acetic acid (Sigma-Aldrich). Optical densities were then read immediately at 570 λ. Each experiment was done in triplicate. Paired *t* test was used to statistically analyze results. When manual count was performed, the same procedure was followed; however, cells were stained with Cell Tracer (according to manufacturer's instructions) and DAPI and manually counted using a microscope. For anti-CCL6 neutralizing experiments, the same protocol was applied; however, anti-CCL6 antibody was added in the appropriate wells (15 µg/ml rat monoclonal MAB487; R&D Systems).

Flow cytometry

Primary macrophages were detached from the plate with Accutase Solution (Thermo Fisher Scientific), and nonspecific antibody binding was prevented by incubating cells with an Fc block (TruStain FcX anti-CD16/32, clone 93). Cells were then

stained with LIVE/DEAD Fixable Viability Dye eFluor 780; BioLegend) 20 min at 4°C, followed by staining with the following antibody mix: F4/80-BV421 clone BM8, CD206-APC clone C068C2, MHC-II-BV40 clone M5/114.15.2, Ly6G BUV786 clone 1A8, and CD11b PE-594 clone M1/70 (BD Biosciences and BioLegend) for 15 min at room temperature. Each antibody was previously titrated to identify the optimal working dilution. Cells were then fixed in 0.05% PFA and acquired using the BD FACSymphony system.

Tumor samples were processed for single-cell suspension. Briefly, tumors were mechanistically dissociated into a solution with 1 mg/ml collagenase V (Gibco BRL, Thermo Fisher Scientific) in DMEM on a rocking platform at 37°C in 5% CO_2 for 1.5 h. Cell suspension was then centrifuged and digested for an additional 5 min with 2.5% trypsin (Gibco BRL, Thermo Fisher Scientific), which was then inactivated by adding complete medium with FBS. Cell suspension was then passed through a syringe needle several times until dissociated and filtered through a 40-µm cell strainer. Cell suspension was then incubated with Fc block, and the same protocol used for primary macrophages was applied. The following antibody mix was used: CD45-BUV563 clone 30Fl1, F480-BV421 clone BM8, CD11b-PE-594 clone M1/70, Ly6G BV786 clone 1A8, Ly6C Alexa Fluor 700 clone HK1.4, CD206 APC clone C068C2, MHC-II BV480 clone M5/114.15.2, CD36 PE clone MM36, CD115 BV711 clone AFS98, CD3 BV650 clone 17A2, PDL1 BV605 clone MIH5, CD4 BUV496 clone GK1.5, CD8 BV805 clone 53-6.7, NK1.1 BUV395 clone PK136, CD45R BV570 clone RA3-6B2, CD25 BB515 clone PC61, CD127 PeCy5 clone A7R34, and KLRG1 PerCp 5.5 clone 2FI (BD Biosciences and BioLegend). For ADFP detection, after extracellular staining, samples were fixed and permeabilized (Foxp3 Transcription Factor Buffer Set; eBioscience) and stained with ADFP antibody (clone PA1-16972; Thermo Fisher Scientific). Subsequently, cells were stained with an appropriate secondary antibody (Alexa Fluor 488, Molecular Probes; Thermo Fisher Scientific). Samples were acquired using a BD FACSymphony system, and data were analyzed using FlowJo software. For sorting experiments, cells were stained for CD45, F4/80, CD11b, Ly6G, and viability dye, and viable macrophages defined as $CD45^+F4/80^+CD11^+Ly6G^-$ cells were sorted using BD FACSAria III.

Mice

All mice were maintained under specific pathogen–free conditions of the Humanitas Clinical and Research Institute, and experiments were performed according to national guidelines approved by the Italian Health Ministry. C57BL/6N and NOD-SCID mice were provided by Charles River. $Pten^{pc-/-}$ and $PbCre^{-/+}$ mice were obtained from The Jackson Laboratory and crossed to obtain $Pten^{pc-/-}$ mice. These mice were then crossed to $Smad4^{pc-/-}$ mice to obtain $Pten^{pc-/-}$; $Smad4^{pc-/-}$ mice. Primers used for genotyping were the following: PbCre forward 5′-CTGAAGAATGGGACAGGCATTG-3′, reverse 5′-CATCACTCG TTGCATCGACC-3′; Pten forward 5′-CAAGCACTCTGCGAACTG AG-3′, reverse 5′-AAGTTTTTGAAGGCAAGATGC-3′; and Smad4 forward 5′-CAGAGTGGGTCTTTCTACCTTAGT-3′, reverse 5′-CAAGCTTTGAGAATGTCTGTGATAG-3′.

For the allograft experiments, 2.5×10^6 $Pten^{-/-}$ or $Pten^{-/-}$; $Smad4^{-/-}$ or $Pten^{-/-}$; $Trp53^{-/-}$; $Smad4^{-/-}$; epithelial cells were injected subcutaneously in the flank of male 8-wk NOD-SCID mice. 10 d after injection, mice were randomized to the treatment groups. Tumor growth was monitored every other day by measuring tumor size with a caliper. αMarco treatment (100 µg/injection for the first two injections and 50 µg/injection for the last three injections, rat anti-mouse Marco antibody, clone ED31 IgG1) or isotype control (anti-rat IgG1) was administered intravenously two times a week for 2 wk. The treatment started 10 d after tumor cell subcutaneous injections in NOD-SCID mice and at week 9 in transgenic mice. Mice were then sacrificed 1 d after the last injection. For HFD experiments, 10 d after subcutaneous cell injection, mice were randomized into two treatments groups: chow diet (control) and HFD diet (45% fat; Mucedola). Food was ad libitum. Mice were sacrificed after 1 mo of dietary treatment. For the combinatorial experiments, docetaxel was administered i.p. at 6 mg/kg every 7 d.

For the orthotopic model, 2.5×10^6 $Pten^{-/-}$ or $Pten^{-/-}$; $Smad4^{-/-}$ cells were injected in one of the anterior lobes of the prostate; the other lobe was injected with saline. Mice were then sacrificed 1.5 mo after injection.

Immunofluorescence

BMDMs were fixed with 4% PFA and then incubated with 2% BSA for 30 min, permeabilized with 0.3% Triton X-100 for 5 min, and then blocked with 2% BSA + NGS for 1 h. Macrophages were then incubated with primary antibody F4/80 (Clone Cl:A3-1; Bio-Rad), followed by secondary antibody (Alexa Fluor 647, Molecular Probes; Thermo Fisher Scientific) and DAPI staining. Coverslips were mounted with FluorSave Reagent (Merck), and samples were acquired using an SP8-II confocal microscope (Leica) with 60× objective and analyzed using ImageJ software. For each experiment, at least three replicates were performed and at least six fields per condition were acquired and quantified by ImageJ. Immunofluorescence was performed on OCT embedded mouse and human tumor samples. 8-µm slices were cut with a cryostat and fixed with 4% PFA. Slices were then blocked with 2% BSA for 30 min, stained for F4/80 (Clone Cl:A3-1) for mouse tissue or for CD68 (Clone KP1; Biocare Medical) for human tissue, MARCO (clone ED31 [Genetex] for mouse tissue or clone LS-B15577 [LSBio] for human tissue) or ADFP (clone PA1-16972; Thermo Fisher Scientific) in 2% BSA, 0.1% Triton X-100, and 5% NGS, followed by secondary antibody and DAPI staining. Slices were mounted with FluorSave Reagent (Merck), and samples were acquired using an SP8-II confocal microscope with 40× objective and analyzed using ImageJ software. The following secondary antibodies were used: Alexa Fluor 647 or 488 (Molecular Probes; Thermo Fisher Scientific). BODIPY 493/503 (Thermo Fisher Scientific) staining was performed according to the manufacturer's instructions.

Histopathology

Tumor size was measured by a caliper, and then the following equation was applied to derive tumor size: size = ($width^2$ × length) / 2. For the prostatic tumors, the size of two anterior lobes was considered. For H&E staining, mouse tumors were fixed in 4% neutral formalin for at least 24 h and embedded in paraffin according to standard procedures. 3 µm was then cut

with a microtome, and H&E staining was performed according to standard protocols. Histology was then evaluated blindly.

Statistical analysis

Statistical analyses were performed using two-tailed unpaired or paired Student's *t* test and one-way ANOVA as specified. Pearson's test was used for the correlation analyses. Values are presented as mean ± SEM (*, $P < 0.05$; **, $P < 0.01$; ***, $P < 0.001$). Data were analyzed using GraphPad Prism 7 software.

Online supplemental material

Fig. S1 shows the scRNA-seq analysis of TAMs in PCa patients and the correlation of MARCO expression with lipid accumulation, Gleason score, and PTEN loss. Fig. S2 shows the characterization of murine lipid-loaded macrophages in vitro and ex vivo. Fig. S3 shows the profiling of the secretome from murine cancer cell lines and the impact of Ccl6 blockade on tumor invasiveness in the transgenic model of PCa. Fig. S4 shows the gating strategies applied to analyze the immune subsets infiltrating the PCa models upon treatment; quantification and immunofluorescence staining of lipid-loaded TAMs are also included. Fig. S5 shows the preclinical trial that tested MARCO blockade in HFD-treated mice; quantification of lipid content in macrophages upon docetaxel treatment is also reported.

Data availability

The complete scRNA-seq and RNA-seq datasets were submitted to Gene Expression Omnibus under accession nos. GSE153892 (raw and processed scRNA-seq data), GSE153975 (raw and processed bulk RNA-seq of TAM in $Pten^{pc-/-}$; $Smad4^{pc-/-}$ murine tumors), and GSE153977 (raw and processed bulk RNA-seq of TAM in HFD mouse models). A token code for data accessibility could be provided to reviewers upon request. The authors declare that all other data supporting the findings of this study are available within this article, its online supplemental material, and from the authors upon request.

Acknowledgments

We thank Dr. Achille Anselmo for cell sorting experiments, Dr. Antonio Sica and Dr. Francesca Consonni for discussion and technical help for flow cytometry experiments, Dr. Fabio Pasqualini and Dr. Fabio Grizzi for immunohistochemistry technical help, and Dr. Chiara Perucchini and Emanuele Di Marco for discussion and technical help. We also thank all the patients enrolled in the study.

This work was supported by Associazione Italiana per la Ricerca sul Cancro (AIRC Start up ID 19141 to D. Di Mitri) and Minsal (Gr-2016-02363531 to D. Di Mitri). D. Di Mitri received funds from AIRC 5x1000 2019-ID 22757. M. Masetti is supported by a fellowship from Fondazione Umberto Veronesi. G. Marelli is supported by a fellowship from Associazione Italiana per la Ricerca sul Cancro (ID 22588) . E. Lugli is supported by Associazione Italiana per la Ricerca sul Cancro (AIRC IG 2017 – ID 20676). J. Brummelman is a recipient of the Associazione Italiana per la Ricerca sul Cancro "Fondo di beneficenza Intesa San Paolo" fellowship. Purchase of the BD FACSymphony A5 has been defrayed in part by Italian Ministry of Health (agreement 82/2015).

Author contributions: M. Masetti performed the experiments. R. Carriero performed the sequencing analysis, interpreted the data, and revised the manuscript. F. Portale, G. Marelli, N. Morina, M. Pandini, M. Iovino, B. Partini, and M.W.H. Chung performed the experiments. M. Erreni supervised the analysis of immunofluorescence data. F. Portale, A. Ponzetta, and J. Brummelman designed the flow cytometry panels and performed the related analysis. E. Magrini gave technical support for the in vivo preclinical trials. F.S. Colombo gave technical support for the FACS sorting. J.M.M. den Haan provided the αMarco neutralizing antibody. C. Peano and J. Cibella performed the RNA-seq. A. Termanini and P. Kunderfranco performed the sequencing analysis. P. Colombo, G. Elefante, M. Lazzeri, R. Hurle, and P. Casale provided the clinical samples from patients and revised the manuscript. E. Lugli designed the flow cytometry panels and revised the manuscript. S. Mukhopadhyay and S. Gordon provided the Marco KO cells, supervised some of the experiments, and revised the manuscript. R.A. DePinho provided the tumor cell lines, reviewed the manuscript, and contributed to writing. D. Di Mitri developed the concept, designed the experiments, designed the flow cytometry panels, interpreted the data, and wrote the manuscript.

Disclosures: R.A. DePinho reported being a Founder and Advisor for Tvardi Therapeutics, Asylia Therapeutics, Nirogy Therapeutics, Stellanova Therapeutics, and Sporos Bioventures. The focus of these companies is not directly related to the content of this manuscript. S. Gordon reported personal fees from Verseau, Myeloid Therapeutics, and Alnylam outside the submitted work. No other disclosures were reported.

Submitted: 9 March 2021
Revised: 27 August 2021
Accepted: 12 October 2021

References

Alimonti, A., C. Nardella, Z. Chen, J.G. Clohessy, A. Carracedo, L.C. Trotman, K. Cheng, S. Varmeh, S.C. Kozma, G. Thomas, et al. 2010. A novel type of cellular senescence that can be enhanced in mouse models and human tumor xenografts to suppress prostate tumorigenesis. *J. Clin. Invest.* 120: 681–693. https://doi.org/10.1172/JCI40535

Aran, D., A.P. Looney, L. Liu, E. Wu, V. Fong, A. Hsu, S. Chak, R.P. Naikawadi, P.J. Wolters, A.R. Abate, et al. 2019. Reference-based analysis of lung single-cell sequencing reveals a transitional profibrotic macrophage. *Nat. Immunol.* 20:163–172. https://doi.org/10.1038/s41590-018-0276-y

Bacci, M., N. Lorito, A. Smiriglia, and A. Morandi. 2021. Fat and furious: Lipid metabolism in antitumoral therapy response and resistance. *Trends Cancer.* 7:198–213. https://doi.org/10.1016/j.trecan.2020.10.004

Baenke, F., B. Peck, H. Miess, and A. Schulze. 2013. Hooked on fat: the role of lipid synthesis in cancer metabolism and tumour development. *Dis. Model. Mech.* 6:1353–1363. https://doi.org/10.1242/dmm.011338

Balaban, S., Z.D. Nassar, A.Y. Zhang, E. Hosseini-Beheshti, M.M. Centenera, M. Schreuder, H.M. Lin, A. Aishah, B. Varney, F. Liu-Fu, et al. 2019. Extracellular fatty acids are the major contributor to lipid synthesis in prostate cancer. *Mol. Cancer Res.* 17:949–962. https://doi.org/10.1158/1541-7786.MCR-18-0347

Batista-Gonzalez, A., R. Vidal, A. Criollo, and L.J. Carreño. 2020. new insights on the role of lipid metabolism in the metabolic reprogramming of

macrophages. *Front. Immunol.* 10:2993. https://doi.org/10.3389/fimmu.2019.02993

Bezzi, M., N. Seitzer, T. Ishikawa, M. Reschke, M. Chen, G. Wang, C. Mitchell, C. Ng, J. Katon, A. Lunardi, et al. 2018. Diverse genetic-driven immune landscapes dictate tumor progression through distinct mechanisms. *Nat. Med.* 24:165–175. https://doi.org/10.1038/nm.4463

Biswas, S.K. 2015. Metabolic reprogramming of immune cells in cancer progression. *Immunity.* 43:435–449. https://doi.org/10.1016/j.immuni.2015.09.001

Calcinotto, A., C. Spataro, E. Zagato, D. Di Mitri, V. Gil, M. Crespo, G. De Bernardis, M. Losa, M. Mirenda, E. Pasquini, et al. 2018. IL-23 secreted by myeloid cells drives castration-resistant prostate cancer. *Nature.* 559:363–369. https://doi.org/10.1038/s41586-018-0266-0

Cao, J., J. Liu, R. Xu, X. Zhu, X. Zhao, and B.Z. Qian. 2017. Prognostic role of tumour-associated macrophages and macrophage scavenger receptor 1 in prostate cancer: a systematic review and meta-analysis. *Oncotarget.* 8:83261–83269. https://doi.org/10.18632/oncotarget.18743

Cassetta, L., and T. Kitamura. 2018. Targeting tumor-associated macrophages as a potential strategy to enhance the response to immune checkpoint inhibitors. *Front. Cell Dev. Biol.* 6:38. https://doi.org/10.3389/fcell.2018.00038

Chen, M., J. Zhang, K. Sampieri, J.G. Clohessy, L. Mendez, E. Gonzalez-Billalabeitia, X.S. Liu, Y.R. Lee, J. Fung, J.M. Katon, et al. 2018. An aberrant SREBP-dependent lipogenic program promotes metastatic prostate cancer. *Nat. Genet.* 50:206–218. https://doi.org/10.1038/s41588-017-0027-2

Dang, Q., Y.A. Chen, and J.T. Hsieh. 2019. The dysfunctional lipids in prostate cancer. *Am. J. Clin. Exp. Urol.* 7:273–280.

Di Mitri, D., M. Mirenda, J. Vasilevska, A. Calcinotto, N. Delaleu, A. Revandkar, V. Gil, G. Boysen, M. Losa, S. Mosole, et al. 2019. Re-education of tumor-associated macrophages by CXCR2 blockade drives senescence and tumor inhibition in advanced prostate cancer. *Cell Rep.* 28:2156–2168.e5. https://doi.org/10.1016/j.celrep.2019.07.068

Ding, Z., C.J. Wu, G.C. Chu, Y. Xiao, D. Ho, J. Zhang, S.R. Perry, E.S. Labrot, X. Wu, R. Lis, et al. 2011. SMAD4-dependent barrier constrains prostate cancer growth and metastatic progression. *Nature.* 470:269–273. https://doi.org/10.1038/nature09677

Dobin, A., C.A. Davis, F. Schlesinger, J. Drenkow, C. Zaleski, S. Jha, P. Batut, M. Chaisson, and T.R. Gingeras. 2013. STAR: ultrafast universal RNA-seq aligner. *Bioinformatics.* 29:15–21. https://doi.org/10.1093/bioinformatics/bts635

Donadon, M., G. Torzilli, N. Cortese, C. Soldani, L. Di Tommaso, B. Franceschini, R. Carriero, M. Barbagallo, A. Rigamonti, A. Anselmo, et al. 2020. Macrophage morphology correlates with single-cell diversity and prognosis in colorectal liver metastasis. *J. Exp. Med.* 217:e20191847. https://doi.org/10.1084/jem.20191847

Dow, M., R.M. Pyke, B.Y. Tsui, L.B. Alexandrov, H. Nakagawa, K. Taniguchi, E. Seki, O. Harismendy, S. Shalapour, M. Karin, et al. 2018. Integrative genomic analysis of mouse and human hepatocellular carcinoma. *Proc. Natl. Acad. Sci. USA.* 115:E9879–E9888. https://doi.org/10.1073/pnas.1811029115

Elshourbagy, N.A., X. Li, J. Terrett, S. Vanhorn, M.S. Gross, J.E. Adamou, K.M. Anderson, C.L. Webb, and P.G. Lysko. 2000. Molecular characterization of a human scavenger receptor, human MARCO. *Eur. J. Biochem.* 267:919–926. https://doi.org/10.1046/j.1432-1327.2000.01077.x

Escamilla, J., S. Schokrpur, C. Liu, S.J. Priceman, D. Moughon, Z. Jiang, F. Pouliot, C. Magyar, J.L. Sung, J. Xu, et al. 2015. CSF1 receptor targeting in prostate cancer reverses macrophage-mediated resistance to androgen blockade therapy. *Cancer Res.* 75:950–962. https://doi.org/10.1158/0008-5472.CAN-14-0992

Georgoudaki, A.M., K.E. Prokopec, V.F. Boura, E. Hellqvist, S. Sohn, J. Östling, R. Dahan, R.A. Harris, M. Rantalainen, D. Klevebring, et al. 2016. Reprogramming tumor-associated macrophages by antibody targeting inhibits cancer progression and metastasis. *Cell Rep.* 15:2000–2011. https://doi.org/10.1016/j.celrep.2016.04.084

González-Chavarría, I., R.P. Cerro, N.P. Parra, F.A. Sandoval, F.A. Zuñiga, V.A. Omazábal, L.I. Lamperti, S.P. Jiménez, E.A. Fernandez, N.A. Gutiérrez, et al. 2014. Lectin-like oxidized LDL receptor-1 is an enhancer of tumor angiogenesis in human prostate cancer cells. *PLoS One.* 9:e106219. https://doi.org/10.1371/journal.pone.0106219

Gordon, S.R., R.L. Maute, B.W. Dulken, G. Hutter, B.M. George, M.N. McCracken, R. Gupta, J.M. Tsai, R. Sinha, D. Corey, et al. 2017. PD-1 expression by tumour-associated macrophages inhibits phagocytosis and tumour immunity. *Nature.* 545:495–499. https://doi.org/10.1038/nature22396

Gordon, J.A., J.W. Noble, A. Midha, F. Derakhshan, G. Wang, H.H. Adomat, E.S. Tomlinson Guns, Y.Y. Lin, S. Ren, C.C. Collins, et al. 2019. Upregulation of scavenger receptor B1 is required for steroidogenic and nonsteroidogenic cholesterol metabolism in prostate cancer. *Cancer Res.* 79:3320–3331. https://doi.org/10.1158/0008-5472.CAN-18-2529

Guan, W., J. Hu, L. Yang, P. Tan, Z. Tang, B.L. West, G. Bollag, H. Xu, and L. Wu. 2019. Inhibition of TAMs improves the response to docetaxel in castration-resistant prostate cancer. *Endocr. Relat. Cancer.* 26:131–140. https://doi.org/10.1530/ERC-18-0284

Hayashi, T., K. Fujita, S. Nojima, Y. Hayashi, K. Nakano, Y. Ishizuya, C. Wang, Y. Yamamoto, T. Kinouchi, K. Matsuzaki, et al. 2018. High-fat diet-induced inflammation accelerates prostate cancer growth via IL6 signaling. *Clin. Cancer Res.* 24:4309–4318. https://doi.org/10.1158/1078-0432.CCR-18-0106

Jaitin, D.A., L. Adlung, C.A. Thaiss, A. Weiner, B. Li, H. Descamps, P. Lundgren, C. Bleriot, Z. Liu, A. Deczkowska, et al. 2019. Lipid-associated macrophages control metabolic homeostasis in a Trem2-dependent manner. *Cell.* 178:686–698.e14. https://doi.org/10.1016/j.cell.2019.05.054

Jamaspishvili, T., D.M. Berman, A.E. Ross, H.I. Scher, A.M. De Marzo, J.A. Squire, and T.L. Lotan. 2018. Clinical implications of PTEN loss in prostate cancer. *Nat. Rev. Urol.* 15:222–234. https://doi.org/10.1038/nrurol.2018.9

Johnson, A.R., Y. Qin, A.J. Cozzo, A.J. Freemerman, M.J. Huang, L. Zhao, B.P. Sampey, J.J. Milner, M.A. Beck, B. Damania, et al. 2016. Metabolic reprogramming through fatty acid transport protein 1 (FATP1) regulates macrophage inflammatory potential and adipose inflammation. *Mol. Metab.* 5:506–526. https://doi.org/10.1016/j.molmet.2016.04.005

Kaneda, M.M., K.S. Messer, N. Ralainirina, H. Li, C.J. Leem, S. Gorjestani, G. Woo, A.V. Nguyen, C.C. Figueiredo, P. Foubert, et al. 2016. PI3Kγ is a molecular switch that controls immune suppression. *Nature.* 539:437–442. https://doi.org/10.1038/nature19834

Katzenelenbogen, Y., F. Sheban, A. Yalin, I. Yofe, D. Svetlichnyy, D.A. Jaitin, C. Bornstein, A. Moshe, H. Keren-Shaul, M. Cohen, et al. 2020. Coupled scRNA-seq and intracellular protein activity reveal an immunosuppressive role of TREM2 in cancer. *Cell.* 182:872–885.e19. https://doi.org/10.1016/j.cell.2020.06.032

Kridel, S.J., F. Axelrod, N. Rozenkrantz, and J.W. Smith. 2004. Orlistat is a novel inhibitor of fatty acid synthase with antitumor activity. *Cancer Res.* 64:2070–2075. https://doi.org/10.1158/0008-5472.CAN-03-3645

Kyi, C., and M.A. Postow. 2016. Immune checkpoint inhibitor combinations in solid tumors: opportunities and challenges. *Immunotherapy.* 8:821–837. https://doi.org/10.2217/imt-2016-0002

Lavin, Y., S. Kobayashi, A. Leader, E.D. Amir, N. Elefant, C. Bigenwald, R. Remark, R. Sweeney, C.D. Becker, J.H. Levine, et al. 2017. Innate immune landscape in early lung adenocarcinoma by paired single-cell analyses. *Cell.* 169:750–765.e17. https://doi.org/10.1016/j.cell.2017.04.014

Lin, E.Y., J.F. Li, L. Gnatovskiy, Y. Deng, L. Zhu, D.A. Grzesik, H. Qian, X.N. Xue, and J.W. Pollard. 2006. Macrophages regulate the angiogenic switch in a mouse model of breast cancer. *Cancer Res.* 66:11238–11246. https://doi.org/10.1158/0008-5472.CAN-06-1278

Lu, X., J.W. Horner, E. Paul, X. Shang, P. Troncoso, P. Deng, S. Jiang, Q. Chang, D.J. Spring, P. Sharma, et al. 2017. Effective combinatorial immunotherapy for castration-resistant prostate cancer. *Nature.* 543:728–732. https://doi.org/10.1038/nature21676

Mantovani, A., F. Marchesi, A. Malesci, L. Laghi, and P. Allavena. 2017. Tumour-associated macrophages as treatment targets in oncology. *Nat. Rev. Clin. Oncol.* 14:399–416. https://doi.org/10.1038/nrclinonc.2016.217

Molgora, M., E. Esaulova, W. Vermi, J. Hou, Y. Chen, J. Luo, S. Brioschi, M. Bugatti, A.S. Omodei, B. Ricci, et al. 2020. TREM2 modulation remodels the tumor myeloid landscape enhancing anti-PD-1 immunotherapy. *Cell.* 182:886–900.e17. https://doi.org/10.1016/j.cell.2020.07.013

Munir, R., J. Lisec, J.V. Swinnen, and N. Zaidi. 2019. Lipid metabolism in cancer cells under metabolic stress. *Br. J. Cancer.* 120:1090–1098. https://doi.org/10.1038/s41416-019-0451-4

Narita, S., T. Nara, H. Sato, A. Koizumi, M. Huang, T. Inoue, and T. Habuchi. 2019. Research evidence on high-fat diet-induced prostate cancer development and progression. *J. Clin. Med.* 8:597. https://doi.org/10.3390/jcm8050597

Netea-Maier, R.T., J.W.A. Smit, and M.G. Netea. 2018. Metabolic changes in tumor cells and tumor-associated macrophages: A mutual relationship. *Cancer Lett.* 413:102–109. https://doi.org/10.1016/j.canlet.2017.10.037

Niu, Z., Q. Shi, W. Zhang, Y. Shu, N. Yang, B. Chen, Q. Wang, X. Zhao, J. Chen, N. Cheng, et al. 2017. Caspase-1 cleaves PPARγ for potentiating the pro-

tumor action of TAMs. *Nat. Commun.* 8:766. https://doi.org/10.1038/s41467-017-00523-6

Novershtern, N., A. Subramanian, L.N. Lawton, R.H. Mak, W.N. Haining, M.E. McConkey, N. Habib, N. Yosef, C.Y. Chang, T. Shay, et al. 2011. Densely interconnected transcriptional circuits control cell states in human hematopoiesis. *Cell.* 144:296–309. https://doi.org/10.1016/j.cell.2011.01.004

Noy, R., and J.W. Pollard. 2014. Tumor-associated macrophages: from mechanisms to therapy. *Immunity.* 41:49–61. https://doi.org/10.1016/j.immuni.2014.06.010

Park, Y.M. 2014. CD36, a scavenger receptor implicated in atherosclerosis. *Exp. Mol. Med.* 46:e99. https://doi.org/10.1038/emm.2014.38

Peck, B., and A. Schulze. 2019. Lipid metabolism at the nexus of diet and tumor microenvironment. *Trends Cancer.* 5:693–703. https://doi.org/10.1016/j.trecan.2019.09.007

Persson, J., E. Degerman, J. Nilsson, and M.W. Lindholm. 2007. Perilipin and adipophilin expression in lipid loaded macrophages. *Biochem. Biophys. Res. Commun.* 363:1020–1026. https://doi.org/10.1016/j.bbrc.2007.09.074

Qian, B.Z., and J.W. Pollard. 2010. Macrophage diversity enhances tumor progression and metastasis. *Cell.* 141:39–51. https://doi.org/10.1016/j.cell.2010.03.014

Rabold, K., M.G. Netea, G.J. Adema, and R.T. Netea-Maier. 2017. Cellular metabolism of tumor-associated macrophages - functional impact and consequences. *FEBS Lett.* 591:3022–3041. https://doi.org/10.1002/1873-3468.12771

Robenek, H., O. Hofnagel, I. Buers, M.J. Robenek, D. Troyer, and N.J. Severs. 2006. Adipophilin-enriched domains in the ER membrane are sites of lipid droplet biogenesis. *J. Cell Sci.* 119:4215–4224. https://doi.org/10.1242/jcs.03191

Robinson, M.D., and A. Oshlack. 2010. A scaling normalization method for differential expression analysis of RNA-seq data. *Genome Biol.* 11:R25. https://doi.org/10.1186/gb-2010-11-3-r25

Salvagno, C., M. Ciampricotti, S. Tuit, C.S. Hau, A. van Weverwijk, S.B. Coffelt, K. Kersten, K. Vrijland, K. Kos, T. Ulas, et al. 2019. Therapeutic targeting of macrophages enhances chemotherapy efficacy by unleashing type I interferon response. *Nat. Cell Biol.* 21:511–521. https://doi.org/10.1038/s41556-019-0298-1

Sebastian de Bono, J., S. Sandhu, and G. Attard. 2011. Beyond hormone therapy for prostate cancer with PARP inhibitors. *Cancer Cell.* 19:573–574. https://doi.org/10.1016/j.ccr.2011.05.003

Sharma, P., and J.P. Allison. 2015. Immune checkpoint targeting in cancer therapy: toward combination strategies with curative potential. *Cell.* 161:205–214. https://doi.org/10.1016/j.cell.2015.03.030

Stoykova, G.E., and I.R. Schlaepfer. 2019. Lipid metabolism and endocrine resistance in prostate cancer, and new opportunities for therapy. *Int. J. Mol. Sci.* 20:2626. https://doi.org/10.3390/ijms20112626

Straub, B.K., B. Gyoengyoesi, M. Koenig, M. Hashani, L.M. Pawella, E. Herpel, W. Mueller, S. Macher-Goeppinger, H. Heid, and P. Schirmacher. 2013. Adipophilin/perilipin-2 as a lipid droplet-specific marker for metabolically active cells and diseases associated with metabolic dysregulation. *Histopathology.* 62:617–631. https://doi.org/10.1111/his.12038

Stuart, T., A. Butler, P. Hoffman, C. Hafemeister, E. Papalexi, W.M. Mauck III, Y. Hao, M. Stoeckius, P. Smibert, and R. Satija. 2019. Comprehensive integration of single-cell data. *Cell.* 177:1888–1902.e21. https://doi.org/10.1016/j.cell.2019.05.031

Subramanian, A., P. Tamayo, V.K. Mootha, S. Mukherjee, B.L. Ebert, M.A. Gillette, A. Paulovich, S.L. Pomeroy, T.R. Golub, E.S. Lander, and J.P. Mesirov. 2005. Gene set enrichment analysis: a knowledge-based approach for interpreting genome-wide expression profiles. *Proc. Natl. Acad. Sci. USA.* 102:15545–15550. https://doi.org/10.1073/pnas.0506580102

Tang, Z., B. Kang, C. Li, T. Chen, and Z. Zhang. 2019. GEPIA2: an enhanced web server for large-scale expression profiling and interactive analysis. *Nucleic Acids Res.* 47(W1):W556–W560. https://doi.org/10.1093/nar/gkz430

Taylor, B.S., N. Schultz, H. Hieronymus, A. Gopalan, Y. Xiao, B.S. Carver, V.K. Arora, P. Kaushik, E. Cerami, B. Reva, et al. 2010. Integrative genomic profiling of human prostate cancer. *Cancer Cell.* 18:11–22. https://doi.org/10.1016/j.ccr.2010.05.026

Trapnell, C., D. Cacchiarelli, J. Grimsby, P. Pokharel, S. Li, M. Morse, N.J. Lennon, K.J. Livak, T.S. Mikkelsen, and J.L. Rinn. 2014. The dynamics and regulators of cell fate decisions are revealed by pseudotemporal ordering of single cells. *Nat. Biotechnol.* 32:381–386. https://doi.org/10.1038/nbt.2859

van Dijk, D., R. Sharma, J. Nainys, K. Yim, P. Kathail, A.J. Carr, C. Burdziak, K.R. Moon, C.L. Chaffer, D. Pattabiraman, et al. 2018. Recovering gene interactions from single-cell data using data diffusion. *Cell.* 174:716–729.e27. https://doi.org/10.1016/j.cell.2018.05.061

Viganò, E., C.E. Diamond, R. Spreafico, A. Balachander, R.M. Sobota, and A. Mortellaro. 2015. Human caspase-4 and caspase-5 regulate the one-step non-canonical inflammasome activation in monocytes. *Nat. Commun.* 6:8761. https://doi.org/10.1038/ncomms9761

Vitale, I., G. Manic, L.M. Coussens, G. Kroemer, and L. Galluzzi. 2019. Macrophages and metabolism in the tumor microenvironment. *Cell Metab.* 30:36–50. https://doi.org/10.1016/j.cmet.2019.06.001

Wan, F., X. Qin, G. Zhang, X. Lu, Y. Zhu, H. Zhang, B. Dai, G. Shi, and D. Ye. 2015. Oxidized low-density lipoprotein is associated with advanced-stage prostate cancer. *Tumour Biol.* 36:3573–3582. https://doi.org/10.1007/s13277-014-2994-6

Wang, G., X. Lu, P. Dey, P. Deng, C.C. Wu, S. Jiang, Z. Fang, K. Zhao, R. Konaparthi, S. Hua, et al. 2016. Targeting YAP-dependent MDSC infiltration impairs tumor progression. *Cancer Discov.* 6:80–95. https://doi.org/10.1158/2159-8290.CD-15-0224

Watt, M.J., A.K. Clark, L.A. Selth, V.R. Haynes, N. Lister, R. Rebello, L.H. Porter, B. Niranjan, S.T. Whitby, J. Lo, et al. 2019. Suppressing fatty acid uptake has therapeutic effects in preclinical models of prostate cancer. *Sci. Transl. Med.* 11:eaau5758. https://doi.org/10.1126/scitranslmed.aau5758

Wei, S.C., J.H. Levine, A.P. Cogdill, Y. Zhao, N.A.S. Anang, M.C. Andrews, P. Sharma, J. Wang, J.A. Wargo, D. Pe'er, and J.P. Allison. 2017. Distinct cellular mechanisms underlie anti-CTLA-4 and anti-PD-1 checkpoint blockade. *Cell.* 170:1120–1133.e17. https://doi.org/10.1016/j.cell.2017.07.024

Wu, H., Y. Han, Y. Rodriguez Sillke, H. Deng, S. Siddiqui, C. Treese, F. Schmidt, M. Friedrich, J. Keye, J. Wan, et al. 2019. Lipid droplet-dependent fatty acid metabolism controls the immune suppressive phenotype of tumor-associated macrophages. *EMBO Mol. Med.* 11:e10698. https://doi.org/10.15252/emmm.201910698

Zhang, Q., Y. He, N. Luo, S.J. Patel, Y. Han, R. Gao, M. Modak, S. Carotta, C. Haslinger, D. Kind, et al. 2019. Landscape and dynamics of single immune cells in hepatocellular carcinoma. *Cell.* 179:829–845.e20. https://doi.org/10.1016/j.cell.2019.10.003

Zilionis, R., C. Engblom, C. Pfirschke, V. Savova, D. Zemmour, H.D. Saatcioglu, I. Krishnan, G. Maroni, C.V. Meyerovitz, C.M. Kerwin, et al. 2019. Single-cell transcriptomics of human and mouse lung cancers reveals conserved myeloid populations across individuals and species. *Immunity.* 50:1317–1334.e10. https://doi.org/10.1016/j.immuni.2019.03.009

JEM

Supplemental material

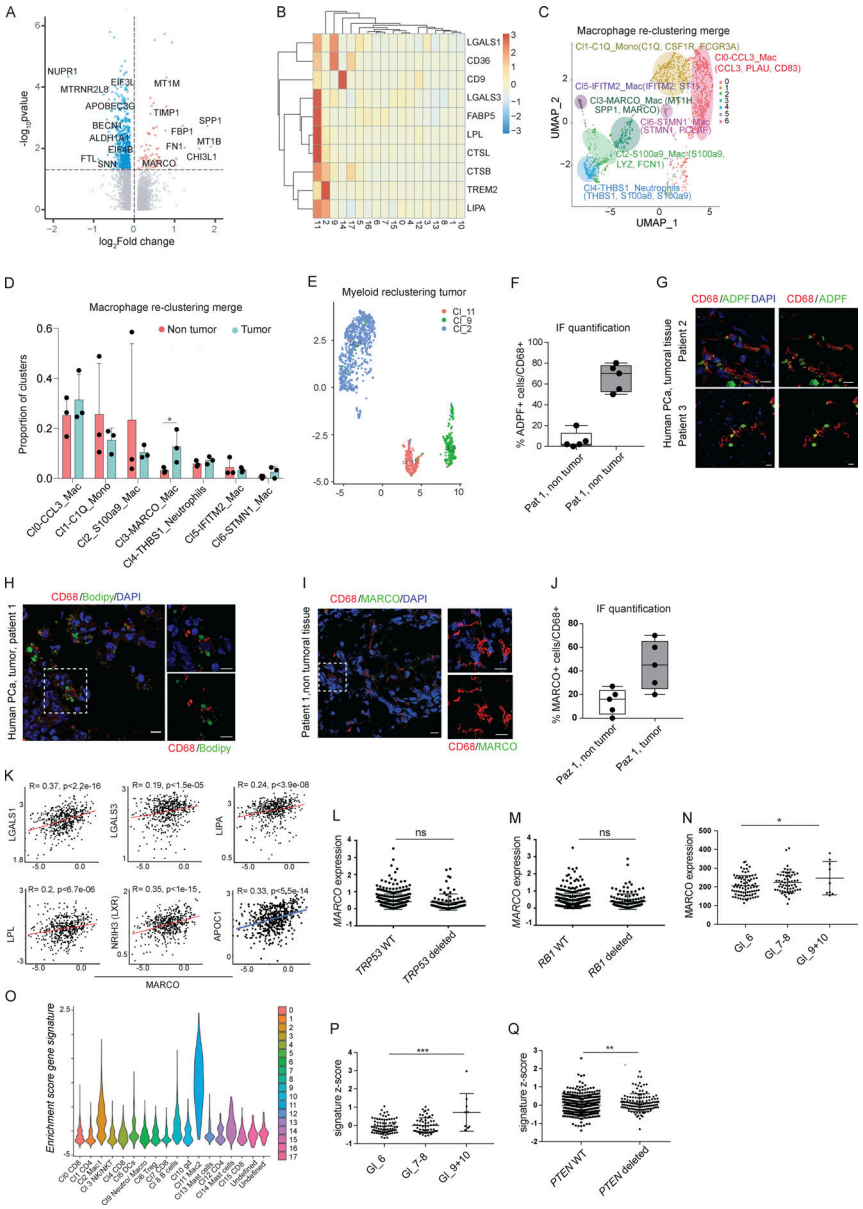

Figure S1. **High-dimensional scRNA-seq analysis of TAMs and correlation of *MARCO* expression with lipid accumulation, Gleason score, and *PTEN* loss. (A)** Volcano plot showing differential expression analysis of Mac2 subsets in the tumor and nontumor tissue. Genes are reported according to their P value and colored by log_2FC values. Three patients were analyzed. **(B)** Heat map reporting Amit gene expression lipid signature along all clusters (Jaitin et al., 2019). **(C)** Uniform manifold approximation and projection (UMAP) reporting reclustering of intratumor and normal adjacent cells of original Cl2, Cl9, and Cl11. **(D)** Proportion of macrophage clusters between tumor and nontumor tissue. Cl3 was significantly enriched in the tumor tissue. **(E)** UMAP showing the correlation between myeloid reclustering and Cl2, Cl11, and Cl9 from the merge analysis. **(F)** Bar graph showing the quantification of ADFP$^+$ cells on CD68$^+$ cells. Five areas per section were considered. **(G)** Representative confocal immunofluorescence images of human PCa. Red-stained CD68$^+$ macrophages colocalized with green-stained ADFP (lipid droplets). Nuclei were counterstained with DAPI (blue). Images were acquired with an SP8-II confocal microscope (Leica) with a 40× objective. Images on the right are 2× digital zoom. Scale bar, 10 mm. **(H)** Representative confocal immunofluorescence images of human PCa. Red-stained CD68$^+$ macrophages colocalized with green-stained BODIPY lipids (lipid droplets). Nuclei are counterstained with DAPI. Images were acquired with an SP8-II confocal microscope with a 40× objective. Images on the right are 2× digital zoom. Scale bar, 10 mm. **(I)** Representative confocal immunofluorescence images of human adjacent nontumor tissue. Red-stained CD68$^+$ macrophages and green-stained MARCO. Images were acquired with an SP8-II confocal microscope with a 40× objective. Images on the right are 2× digital zoom. Scale bar, 10 mm. **(J)** Bar graph showing the quantification of Fig. 3 B (tumor) and I (nontumor). Five areas per section have been considered. **(K)** Graphs showing the Pearson's correlations of gene expression between *MARCO* and lipid-related genes in PCa patients in the TCGA cohort. **(L)** Correlation of *MARCO* gene expression with *TRP53* loss in the TCGA cohort. **(M)** Correlation of *MARCO* gene expression with RB1 loss in the TCGA cohort. **(N)** Correlation of MARCO gene expression with Gleason score in PCa patients from the Taylor dataset. Unpaired *t* test ($P \leq 0.05$). **(O)** Violin plot representing gene signature score derived from MARCO_Mac cluster along the different infiltrating immune subsets. **(P)** Correlation of MARCO_Mac gene signature with Gleason score in PCa patients from the Taylor dataset. Gene signature expression is provided as normalized *z* score. Unpaired *t* test ($P \leq 0.0001$). **(Q)** Correlation of MARCO_Mac gene signature with *PTEN* loss in the TCGA cohort. Gene signature expression is provided as normalized *z* score. Data in F–J, L–N, and P–Q are expressed as mean ± SD. Student's *t* test was performed (D, L–N, P, and Q). *, $P < 0.05$; **, $P < 0.01$; ***, $P < 0.001$. Gl, Gleason; IF, immunofluorescence.

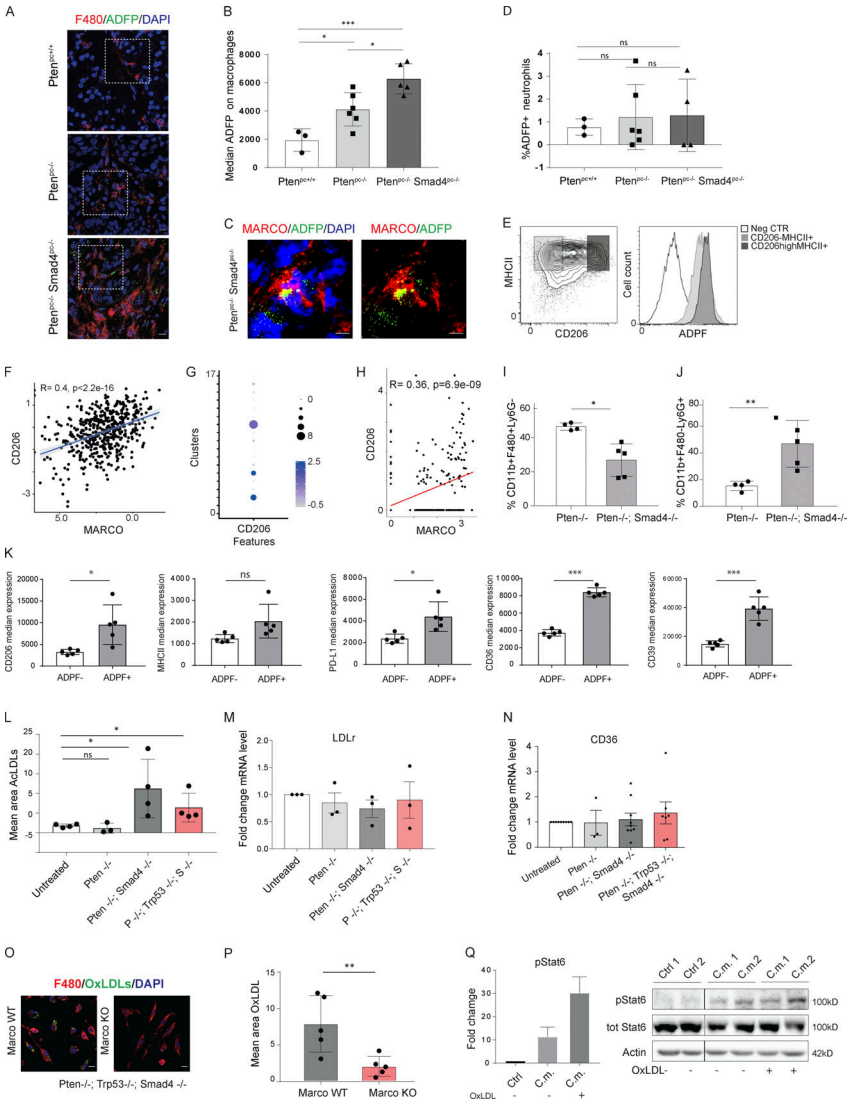

Figure S2. **Analysis of lipid-loaded TAMs in vivo and in vitro. (A)** Representative confocal immunofluorescence images of tumor anterior prostate lobes from WT (Pten$^{pc+/+}$), Pten$^{pc-/-}$, and Pten$^{pc-/-}$; Smad4$^{pc-/-}$ mice. Red-stained F4/80^{+} macrophages colocalized with green-stained ADFP lipid droplets in the Pten$^{pc-/-}$; Smad4$^{pc-/-}$ tumors. Images were acquired with an SP8-II confocal microscope (Leica) with a 40× objective. Nuclei were counterstained with DAPI (blue). Scale bar, 10 µm. **(B)** Median fluorescence intensity of ADFP in TAMs in prostates from WT (Pten$^{pc+/+}$) mice or Pten$^{pc-/-}$ and Pten$^{pc-/-}$; Smad4$^{pc-/-}$ transgenic animals. Mean ± SE are shown. *n* = 3 for WT (Pten$^{pc+/+}$) prostates, *n* = 6 for Pten$^{pc-/-}$, and *n* = 5 for Pten$^{pc-/-}$; Smad4$^{pc-/-}$ tumors. **(C)** Representative confocal immunofluorescence images of tumor anterior prostate lobes from Pten$^{pc-/-}$; Smad4$^{pc-/-}$ mice. Red-stained MARCO^{+} macrophages colocalize with green-stained ADFP lipid droplets in the Pten$^{pc-/-}$; Smad4$^{pc-/-}$ tumors. Images were acquired with an SP8-II confocal microscope with a 40× objective. Displayed are 2× digital zoom. Nuclei were counterstained with DAPI (blue). Scale bar, 5 µm. **(D)** Frequency of ADFP^{+} neutrophils in prostates from WT (Pten$^{pc+/+}$) mice or Pten$^{pc-/-}$ and Pten$^{pc-/-}$; Smad4$^{pc-/-}$ transgenic animals. **(E)** CD206 and MHC-II expression by lipid-loaded TAMs. The expression of the two markers was evaluated in ADFP^{+} TAMs. Increased expression of CD206 correlates with higher expression of ADFP. **(F)** Graph showing the Pearson's correlation between *MARCO* and *CD206* (*MRC1*) gene expression in TCGA cohort. **(G)** Graph showing the percentage and average expression of *CD206* (*MRC1*) in the single-cell–derived human dataset. **(H)** Graph showing the Pearson's correlation between *MARCO* and *CD206* gene expression in the single-cell–derived human dataset. **(I and J)** Analysis of TAMs and neutrophils in the Pten$^{-/-}$ and Pten$^{-/-}$; Smad4$^{-/-}$ orthotopic models. Frequency of TAMs (I) and of neutrophils gated on CD45^{+} cells (J). **(K)** Bar graphs based on FACS analysis showing the expression of macrophage pivotal markers on ADFP^{+} and ADFP^{-} tumor-infiltrating macrophages. **(L)** Bar graph showing the quantification of green-stained acLDL uptake in red-stained F4/80 stained macrophages exposed to different tumor CM. At least three independent experiments were quantified. Mean areas of acLDL labeling per cell ± SE are shown. **(M)** Quantitative RT-PCR of LDL receptor (LDLr) gene expression in primary macrophages exposed to different tumor CM. No significant differences could be detected among conditions. FC was calculated on untreated macrophages as control. All the experiments were conducted in at least three biological replicates. Student's *t* test was performed on ΔCTs. **(N)** Quantitative RT-PCR of *CD36* gene expression in primary macrophages exposed to different tumor CM. FC was calculated on untreated macrophages as control. *n* = 4 for untreated, Pten$^{-/-}$; Smad4$^{-/-}$, and Pten$^{-/-}$; Trp53$^{-/-}$; Smad4$^{-/-}$, and *n* = 3 for Pten$^{-/-}$. **(O and P)** Representative confocal immunofluorescence images and quantification of green-stained oxLDL uptake in red-stained F4/80 stained *Marco* WT and *Marco* KO macrophages exposed to Pten$^{-/-}$; Trp53$^{-/-}$; Smad4$^{-/-}$ tumor CM. Images were acquired on an SP-II confocal microscope with a 60× objective. Scale bar, 10 µm. *n* = 5. Mean area of oxLDL staining per cell ± SE is shown. **(Q)** Western blot image and bar graph showing the expression of total Stat6 and phosphorylated Stat6 on macrophages exposed to oxLDL. Student's *t* test was performed (B, D, I–N, and P) *, P < 0.05; **, P < 0.01; ***, P < 0.001. CTR/Ctrl, control; Neg, negative. Data are expressed as mean ± SD.

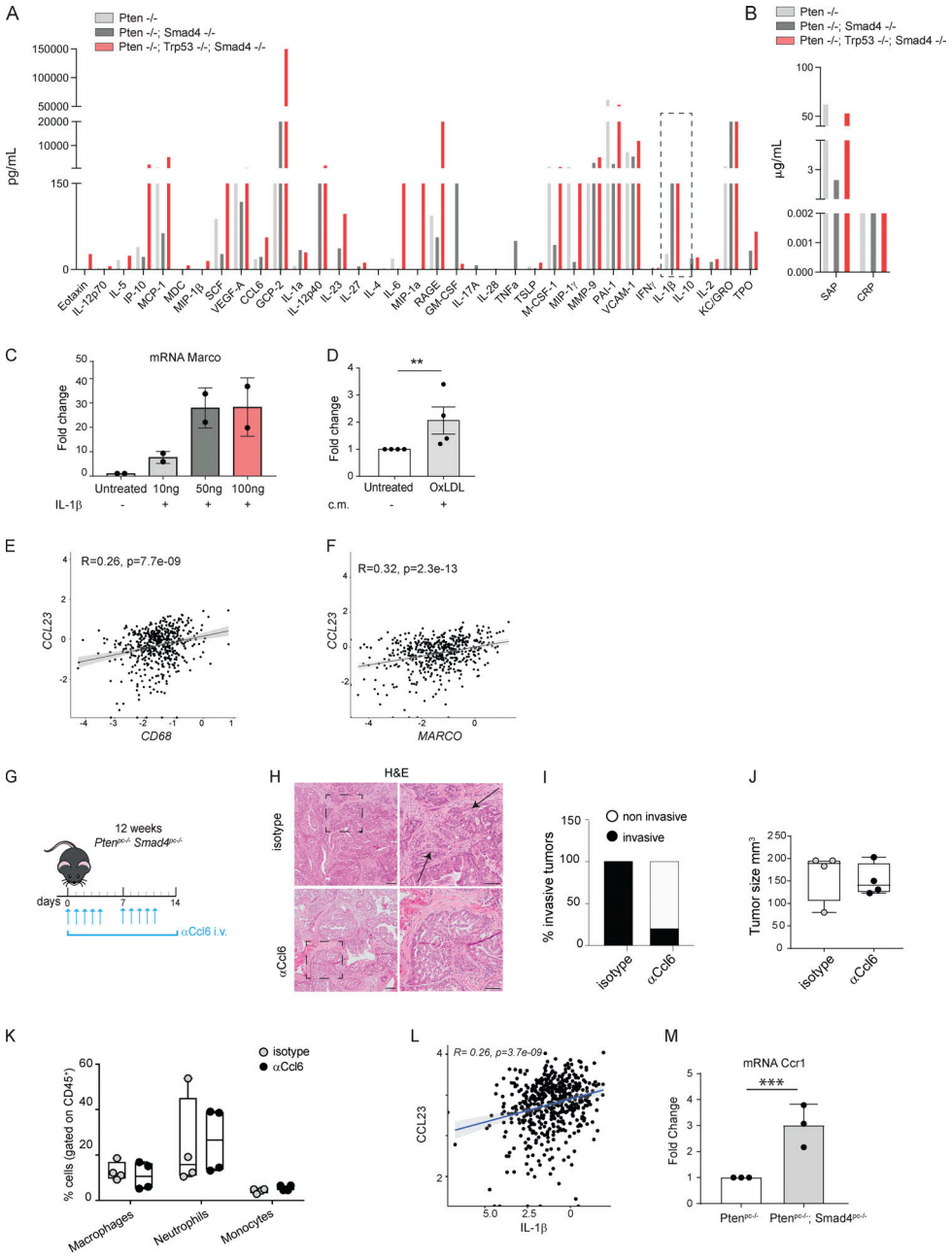

Figure S3. **Analysis of the secretome from murine cancer cell lines and impact of Ccl6 blockade on tumor invasiveness in PCa. (A and B)** Secretome analysis of CM derived from tumor cell lines. CM were collected from Pten$^{-/-}$, Pten$^{-/-}$; Smad4$^{-/-}$, and Pten$^{-/-}$; Trp53$^{-/-}$; Smad4$^{-/-}$ cell lines and concentrated 1:5 in Amicon Ultra Centrifugal Filter Units, and then a multiplex ELISA analyzing 42 different cytokines (Proteome Rodent MAP 4.0; Myriad) was performed. IL-1β expression was higher in metastatic CM (Pten$^{-/-}$; Smad4$^{-/-}$ versus Pten$^{-/-}$; Trp53$^{-/-}$; Smad4$^{-/-}$) versus nonmetastatic one (Pten$^{-/-}$). n = 2. **(C)** Quantitative RT-PCR analysis on primary macrophages treated with different doses of IL-1β. *Marco* expression rose with increasing concentration of IL-1β (n = 2). **(D)** Migration assay. Pten$^{-/-}$; Smad4$^{-/-}$ cells were co-cultured in transwell chambers with primary macrophages previously exposed to tumor CM (Pten$^{-/-}$; Smad4$^{-/-}$) and loaded or not with oxLDLs (10 μg) for 15 h. Migrated cells on the bottom side of the membrane were stained with Cell Tracker Dye for better visualization, and nuclei were stained with DAPI. Cells were manually counted using a microscope. **(E)** Pearson's correlation showing positive association between *CCL23* (ortholog of murine *Ccl6*) and *CD68* in the human PCa TCGA dataset. Gene expression values are provided as FPKM. **(F)** Pearson's correlation showing positive association between *CCL23* and *MARCO* in the human PCa TCGA dataset. Gene expression values are provided as FPKM. **(G)** Schematic of αCcl6 treatment in Pten$^{pc-/-}$; Smad4$^{pc-/-}$ mice. Mice at 9 wk of age were either treated with αCcl6 antibody or with an isotype control. n = 4 mice treated with anti-Ccl6, and n = 4 mice treated with isotype control. Mice were sacrificed at day 15. **(H)** Representative images of H&E staining of anterior prostate lobes from Pten$^{pc-/-}$; Smad4$^{pc-/-}$ mice treated with anti-Ccl6 or isotype control. Images were acquired using a VS120 dotSlide Microscope (Olympus) with a 20× objective. Scale bar, 200 μm (100 μm for digital zoom). Arrows are pointing at invasive areas. **(I)** Bar graph showing the quantification of tumor invasiveness. **(J)** Tumor size in Pten$^{pc-/-}$; Smad4$^{pc-/-}$ mice treated with anti-Ccl6 antibody or isotype control. Measures were taken on the day of sacrifice. **(K)** Percentage of myeloid subsets gated on CD45$^+$ cells. **(L)** Graph showing Pearson's correlation between *IL-1β* and *CCL23* in TCGA cohort. **(M)** Bar graph showing the gene expression of Ccr1 on cells isolated from Pten$^{pc-/-}$ and Pten$^{pc-/-}$; Smad4$^{pc-/-}$ tumors. Student's t test was performed (D, J, K, and M). **, P < 0.01; ***, P < 0.001. CRP, C-reactive protein; SAP, serum amyloid P component. Data in C, D, H, and M are expressed as mean ± SD.

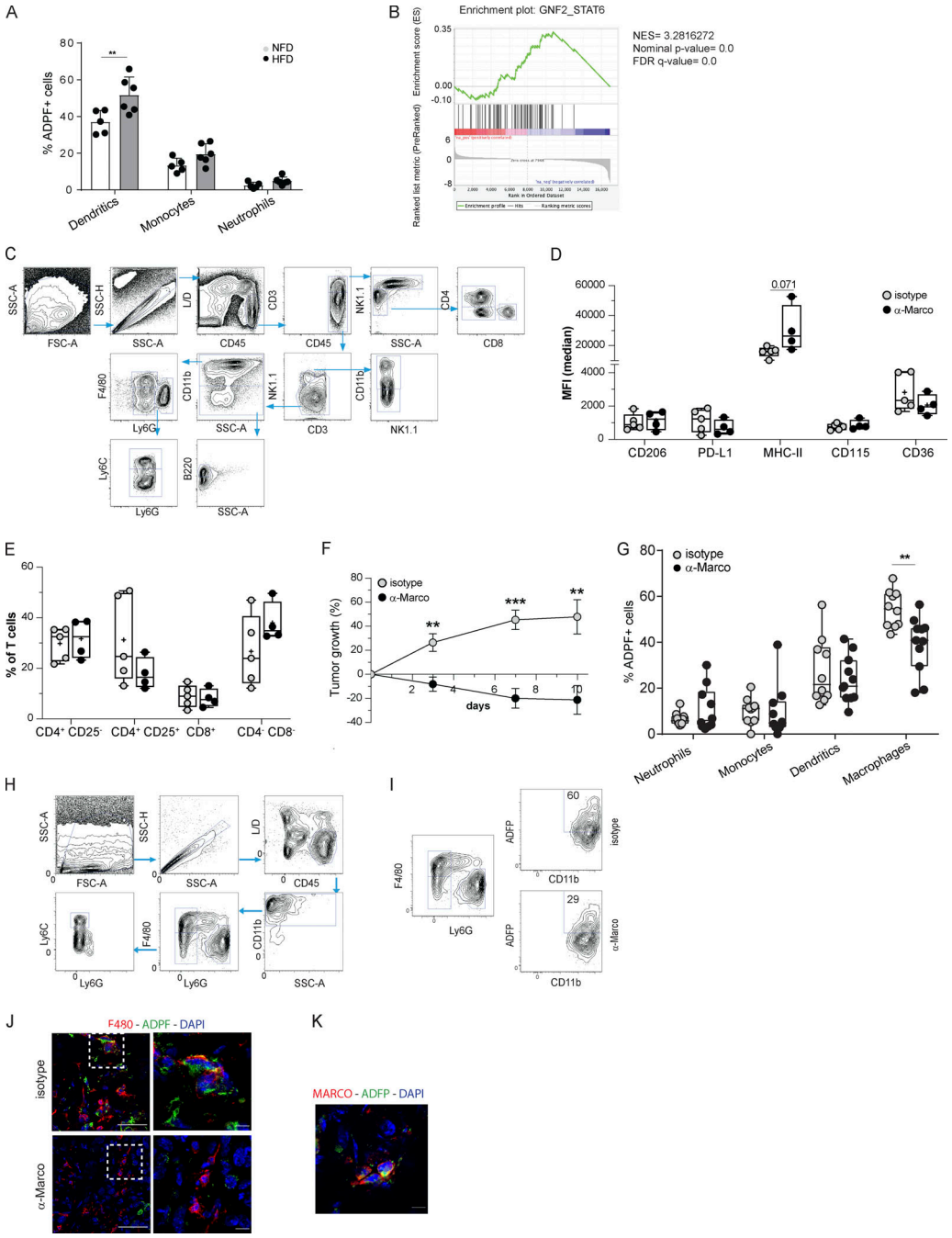

Figure S4. **Analysis of the immune infiltrate in vivo. (A)** Bar graph showing the percentage of ADFP⁺ myeloid subsets gated on CD45. *n* = 5 mice on NFD, and *n* = 6 mice on HFD. **(B)** GSEA showing the enrichment of the GNF2_Stat6 pathway in macrophages sorted from HFD mice versus NFD mice. **(C–E)** Analysis of the immune infiltrate in Pten$^{pc-/-}$; Smad4$^{pc-/-}$ tumors from mice treated with αMarco (*n* = 4) or with isotype control (*n* = 5). Gating strategy used to analyze different immune cell subsets in Pten$^{pc-/-}$; Smad4$^{pc-/-}$ tumors (C) and frequency of immune subsets (D and E). **(E)** Frequency of different T cell subsets in Pten$^{-/-}$; Smad4$^{-/-}$ tumors from mice treated with αMarco or with isotype control. CD4⁺ T cells are identified as CD4⁺CD25⁻; Treg cells as CD4⁺CD25⁺, and unconventional T cells as CD4⁻CD8⁻. **(F)** Curve showing the growth of subcutaneous tumors from NOD-SCIDγ mice treated with αMarco antibody or isotype control. **(G)** Bar graph showing the percentage of ADFP⁺ myeloid cells infiltrating the tumors. **(H and I)** Gating strategy used to identify lipid-loaded TAMs in subcutaneous tumors from NOD-SCIDγ mice treated with αMarco antibody or isotype control. Lipid-loaded TAMs are ADFP⁺. **(J)** Representative confocal immunofluorescence images of subcutaneous tumors from NOD-SCIDγ mice injected subcutaneously with Pten$^{-/-}$; Smad4$^{-/-}$ cells. Red-stained F4/80⁺ macrophages colocalize with green-stained ADFP lipid droplets. Nuclei are counterstained with DAPI (blue). Images were acquired with an SP8-II confocal microscope (Leica) with a 40× objective. Images on the right are 2× digital zoom. Scale bar, 50 µm (10 µm for the digital zoom). **(K)** Representative confocal immunofluorescence image of subcutaneous tumors from NOD-SCIDγ mice injected subcutaneously with Pten$^{-/-}$; Smad4$^{-/-}$ cells. Red-stained Marco⁺ macrophages colocalized with green-stained ADFP lipid droplets. Nuclei are counterstained with DAPI (blue). Images were acquired with an SP8-II confocal microscope with a 40× objective. Scale bar, 10 µm. Student's *t* test was performed (A and D–G), **, P < 0.01; ***, P < 0.001. FDR, false discovery rate; FSC-A, forward scatter area; L/D, length-to-diameter ratio; MFI, median fluorescence intensity; NES, normalized enrichment score; SSC-A, side scatter area; SSC-H, side scatter height. Data in A, D, E, and G are expressed as mean ± SD.

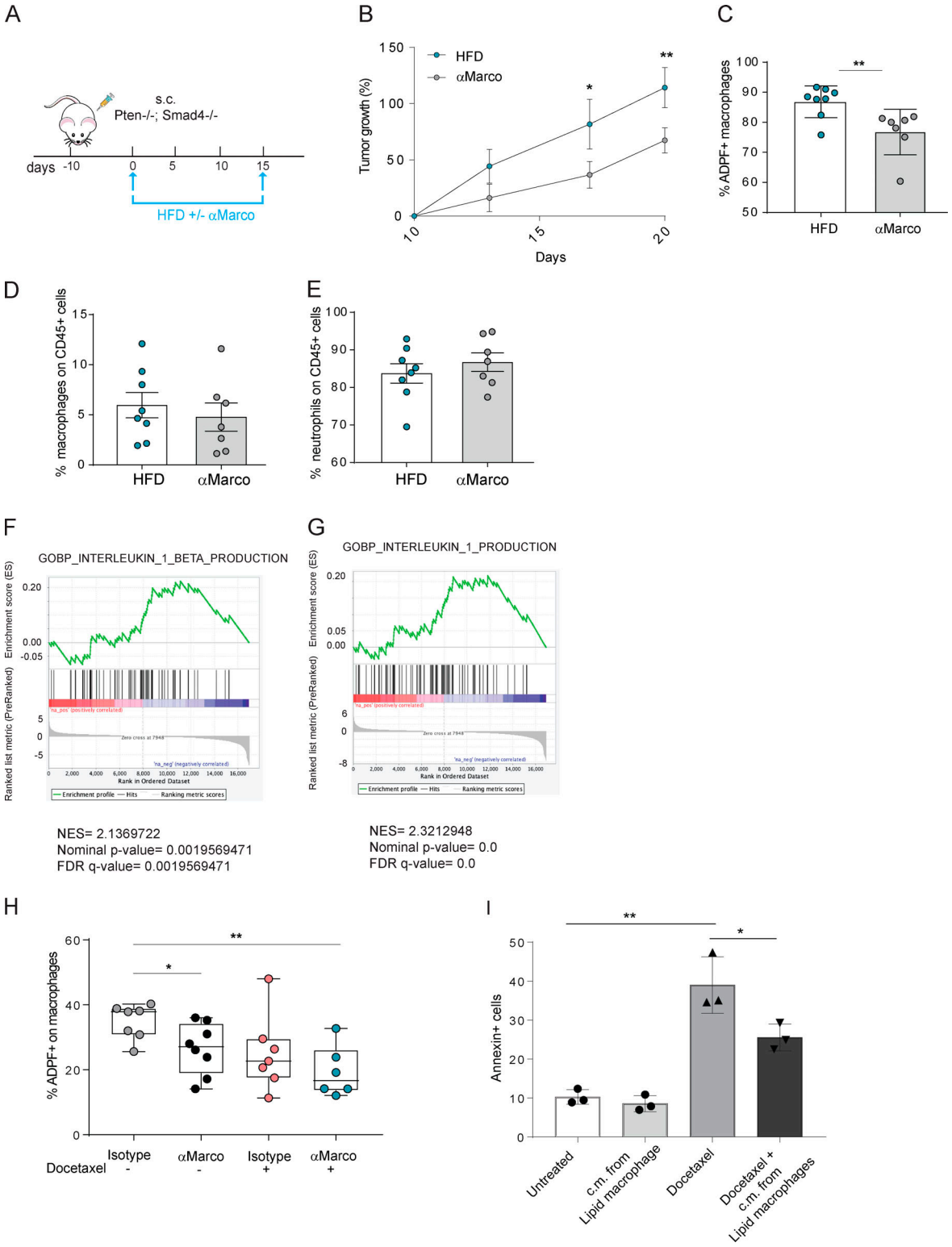

Figure S5. **Marco blockade hinders tumor growth in HFD-treated mice and synergizes with docetaxel in a PCa model. (A)** Schematic of αMarco treatment in tumor-bearing mice exposed to HFD or to NFD as control. Mice were exposed to HFD and NFD and either treated with αMarco antibody or with an isotype control for 15 d. *n* = 7 mice treated with anti-Ccl6, and *n* = 8 mice treated with isotype control. Mice were sacrificed at day 15. **(B)** Curve showing the growth of subcutaneous tumors. **(C)** Bar graph showing the percentage of ADFP$^+$ TAMs gated on CD45$^+$ cells. **(D and E)** Bar graphs showing the frequency of total macrophages and of neutrophils infiltrating the tumors. **(F and G)** GSEA of the Gene Ontology Biological Process (GOBP)_IL-1β production and GOBP_IL-1 production on tumor cells from HFD- and NFD-fed mice. **(H)** Bar graph showing the percentage of ADFP$^+$ TAMs gated on CD45$^+$ cells. **(I)** Bar graph showing the percentage of annexin$^+$ prostate tumor cells (Pten$^{-/-}$; Smad4$^{-/-}$ cell line) exposed to docetaxel in the presence or absence of CM from lipid-loaded macrophages. Student's *t* test was performed (B–E, H, and I). *, P < 0.05; **, P < 0.01. FDR, false discovery rate; NES, normalized enrichment score. Data are expressed as mean ± SD.